Waste and Biomass Valorization
https://doi.org/10.1007/s12649-025-02991-0

ORIGINAL PAPER

Evaluation of Different Classes of Additives on Ash Melting Characteristics of Garden Grass Waste

Mubashra Latif[1] · **John Graham Brammer**[1] · **John Morris**[1]

Received: 19 October 2024 / Accepted: 22 February 2025

Abstract

In this work, the ash melting characteristics of crude garden grass waste (GGW) and its additive modulated mixtures were evaluated in a laboratory scale furnace by combusting the samples. For the purpose of understanding and rationalising the complex ash transformation characteristics of crude and additive modulated GGW samples in high-temperature thermochemical units, comprehensive theoretical knowledge and compositional ternary phase diagrams have been utilised in conjunction with the visual evaluation of the sintering degree of ash residues, coupled with their morphology and microchemistry results determined by the SEM–EDX and XRD analysis. This work proved that both raw and calcined eggshells can be utilised as Ca-rich anti-sintering additives as a substitute for commercially available additives such as lime and limestone for the enhancement of melting characteristics of low-melting garden grass ash. Kaolin exhibited the best anti-sintering characteristics for the elimination of ash melting of garden grass waste among all the additive mixtures tested, while no synergistic effects were observed in the Ca-rich and P-rich additive mixtures compared to their pure steams.

Graphical Abstract

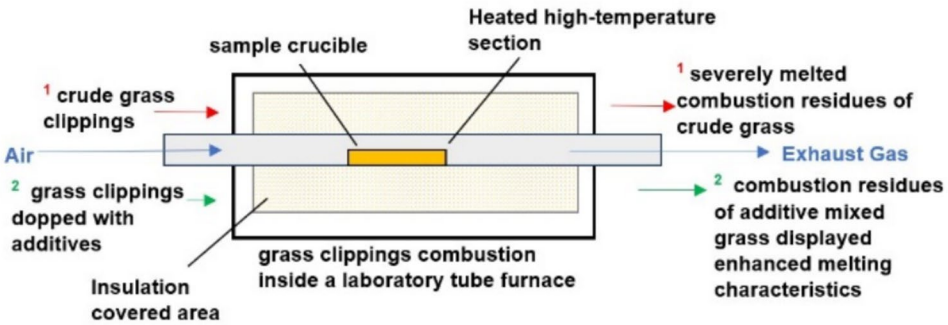

Keywords Garden grass waste · Ash melting · Ash sintering · Eggshell waste · Biomass additives · Biomass combustion

Abbreviations

ADP	Ammonium dihydrogen phosphate
HTA	High temperature ash
GGW	Garden grass waste
EFB	Empty fruit bunch
HHV	Higher heating value
HAB	Herbaceous and agricultural biomass
UA	Ultimate analysis
HAG	Herbaceous and agricultural grass
PA	Proximate analysis
HAR	Herbaceous and agricultural residues
SEM	Scanning electron microscopy
HAS	Herbaceous and agricultural straws
EDX	Energy dispersive spectrometer
TPD	Ternary phase diagrams

✉ John Morris
john.morris@chester.ac.uk

Mubashra Latif
drmlatif@outlook.com

John Graham Brammer
john.brammer@btinternet.com

[1] School of Natural Sciences, University of Chester, Parkgate Campus, Chester CH1 4BJ, England, UK

Published online: 07 March 2025

XRD	Powder X-ray diffraction
AFT	Ash fusion temperature
XRF	X-ray fluorescence
PM	Particulate matter
ICDD	International centre for diffraction data
VM	Volatile matter content
IDT	Initial deformation temperature
FC	Fixed carbon
CES	Calcined eggshells
A	Ash content
LS	Limestone
RIR	Reference intensity ratio
RES	Raw eggshells
Mis	Miscanthus
S1	Sample containing raw garden grass waste (GGW)
S7	Sample containing GGW with 4 wt% RES
S2	Sample containing GGW with 4 wt% lime
S8	Sample containing GGW with 8 wt% RES
S3	Sample containing GGW with 4 wt% CES
S9	Sample containing GGW with 4 wt% kaolin
S4	Sample containing GGW with 8 wt% CES
S10	Sample containing GGW with 8 wt% kaolin
S5	Sample containing GGW with 4 wt% limestone
S11	Sample containing GGW with 4 wt% ADP
S6	Sample containing GGW with 8 wt% limestone
S12	Sample containing GGW with 8 wt% ADP
S13	Sample containing GGW with 4 wt% CES and 4 wt% ADP
TGA	Thermogravimetric analyser
ICP-MS/OES	Inductively coupled plasma mass spectrometry/optical emission spectroscopy

Statement of Novelty

The valorisation of abundantly available grassland in biomass thermochemical systems can help significantly decrease the carbon footprint of world energy systems. However, like other herbaceous biomass, due to problematic composition, the ash of grass clippings severely melts in high-temperature systems (like combustors, gasifiers, etc.), which leads to blockage and damage to the system internals. There is no data in the literature detailing the ash composition of garden grass clippings and how it varies with adding various additives. This work attempts to fill this literature gap by using XRD and SEM-EDS techniques. The ash composition results reported in this work could be used to gain deeper insights into the underlying melting mechanisms of garden grass ash, advancing the database of LCA models and simulation tools and ash composition-based phase diagrams. This work also analyses if eggshell waste could potentially be used as an alternative to Ca-rich commercial anti-sintering additives and if any synergistic effects could be achieved by the simultaneous addition of Ca and P-based additives, which could enhance the meting characteristics of grass waste.

Introduction

In recent years, there has been a rising interest in the evaluation of the applicability of herbaceous biomass (especially as the mixtures of naturally grown grassland biomass and grass cuttings) for bioenergy purposes [1–4]. Their shorter life cycles, resilient traits, limited agricultural requirements with higher yields, and the innate ability to be grown cost-effectively anywhere with minimal or no effort make them more environmentally and economically beneficial among the range of other feedstocks available [5, 6]. However, published literature shows that the comparatively higher levels of K, P, Cl, S, and Si observed in the ash of herbaceous biomass tend to form low-melting potassium-rich silicates and phosphates at elevated temperatures (< 700 °C) [7], which are typical in biomass gasification and combustion systems [3, 8]. This ash melting presents significant challenges inside biomass reactors, like forming corrosive alkali-rich aerosols, deposits, and slagging (including clinker formation) on convective heat transfer surfaces, reactor grates, and fuel bed particles [3, 9]. The future of biomass-driven systems and the production of renewable energy at large could be dramatically changed if these challenges posed by the undesirable ash matter behaviour of herbaceous biomass could be avoided by modifying the fuel ash composition through (1) leaching problematic minerals, (2) mixing appropriate additives or (3) blending biomass streams of different qualities [9, 10].

The energy input required to dry the leached biomass before utilisation in thermochemical conversion systems and the increasing challenges associated with the supply of water resources, especially in many arid and remote regions, makes the utilisation of water-based leaching and biomass demineralisation on the whole unsustainable in the longer run.

Additives help adjust the chemical composition of poor-quality herbaceous biomass fuels and improve the ash-related issues by adsorbing corrosive aerosol vapours on their porous particles and by chemically reacting with ash constituents, forming high melting compounds [9]. According to the contained reactive compounds, additives are classified as phosphorous-based additives (such as H_3PO_3, $NH_4H_2PO_4$ (ADP), and $Ca(H_2PO_4)_2$ (CPM)

etc.), aluminium–silicate based additives (such as kaolin ($Al_2Si_2O_5(OH)_4$), halloysite ($(Al_4(OH)_8Si_4O_{10}\cdot 10H_2O$), zeolites, emathlite, and bentonite etc.), calcium-based additives (limestone, lime (CaO), calcite ($CaCO_3$), dolomite $CaMg(CO_3)_2$), and calcium hydroxide ($Ca(OH_2)$) etc.), and sulphur-based additives (such as $(NH_4)_2SO_4$, $Fe_2(SO_4)_3$, $Al_2(SO_4)_3)_9$.

Each additive has a different ash chemistry. An additive that may work well for one biomass may worsen the thermal processing characteristics of others. An additive's ability to reduce ash-related problems is significantly influenced by its added amount, the way it is added into the biomass system, the reaction atmosphere (process temperature and residence time), and the process design features [11]. Adding the additive in the right amount is the most critical parameter. Although in literature, additives have been used from minute to relatively large amounts (generally between 1 and 20 wt%), it is sensible to keep their amount as low as possible to avoid high operational costs ascribed to their purchase and increased ash handling [11]. It is noteworthy that additives are effective only when used within a specific percentage range, and they do not induce any noticeable improvement in biomass ash fusion characteristics if used outside that range. In fact, their excessive addition may negatively impact the system by worsening the ash-slagging tendency [11]. For these reasons, testing the anti-sintering characteristics of prospective additives at the laboratory scale for each biofuel application is a prerequisite before approving their mass utilisation for an industrial-scale facility. This practice makes the additive's selection process much easier, and it helps gain deeper insights into the complex ash transformation reactions taking place in each additive system [11], which could not be predicted with accuracy otherwise.

Modifying the composition of challenging herbaceous biofuels via blending with high quality biomass streams is evidenced to be more efficient in reducing emissions and blended assortments would always sinter to some extent even if the woody feedstock content is significantly higher (sometimes even over 70%) unless it is coupled with additivation [11]. Since having a share of over 50–70% of woody biomass in a feedstock blend would jeopardize the economic benefit of utilising herbaceous streams in biomass systems. Therefore, mixing additives into biomass is the most environmentally and economically sustainable option for successfully employing low-quality biomass feedstocks in biomass gasification and combustion systems.

Though a few studies investigated the ash melting characteristics of garden grass waste in raw [3], demineralized [12], and kaolin-modulated [13] mixtures at high-temperature systems, but they have not detailed the ash composition of grass clippings and how that transforms when the relative ratio of the problematic elements is changed through additivation. The knowledge of the chemical composition of combustion ash residues from crude garden grass waste and how it transforms when the relative ratio of the problematic elements is changed through additivation is indispensable for the efficient valorisation of grass cuttings in biomass-driven heat and power units. Therefore, this study focuses on thoroughly investigation of the ash melting features of garden grass waste in a laboratory furnace with and without commercially available additives such as lime, limestone, ammonium dihydrogen phosphate and kaolin. SEM–EDS and XRD techniques have been used to gain deeper insights into the distinctive reaction chemistry of the combustion residues of the additive modulated garden grass waste ash mixtures. This study also attempts to investigate the suitability of raw and calcined eggshell waste as a substitute for commercially available Ca-rich additives in the biomass industry.

Due to the compositional similarity of eggshells to limestone, eggshell waste has been previously successfully used as a promising catalyst in bioenergy applications such as biodiesel production, and wood and coal gasification systems in calcined form in particular [14]. It has been found to facilitate tar and char conversion in gasification systems and the enhancement of the yield of gaseous products (H_2 in particular), but to the author`s knowledge, no studies have ever explored in-depth the impact of eggshell waste on the anti-sintering and ash phase transformation characteristics of garden grass waste. The evaluation of the impact of eggshell waste on the ash transformation characteristics of garden grass waste in comparison to the range of different additives would not only open new avenues in decreasing additives-related costs in the biomass industry but would also help solve the disposal and organic pollution issues surrounding the global poultry industry [15].

Materials and Methods

The following sections detail the methods and procedures adopted for preparing feedstocks and samples for the combustion experiments for this work and the subsequent analysis of their combusted residues.

Feedstock and Additives

Garden grass waste (GGW), which also contained a small fraction of leaves, were obtained as yard trimmings in a very wet and muddy state during the winter months. A laboratory electric dryer was used to dry wet GGW at 105 °C for 24 h. Once dried, a representative and homogeneous sample was sorted which was then used for the sample characterization and combustion experiments.

The substances tested as anti-sintering additives for GGW included: calcium oxide, limestone, ammonium dihydrogen phosphate, kaolin, raw eggshells, and calcined eggshells. None of the additives tested required drying for experimentation except for the eggshells, which were received in a wet form and were dried at 110 °C for 24 h in a laboratory electric heating oven. Dried eggshells were subsequently ground into a fine powder in a blender. A part of the representative sample was used in raw form while a portion of the dried eggshell sample was calcined into lime (CaO) by heating in air at 900 °C for 2 h in a laboratory furnace [14] to evaluate the anti-sintering characteristics of calcined eggshells. Air was used instead of an inert atmosphere for calcination of the eggshells as it would be cheaper for heat treatment of eggshells at a large scale.

Table 1 Samples and their abbreviations (wt% on dry basis)

Samples	
Raw garden grass waste (GGW)	S1
GGW with 4 wt% lime	S2
GGW with 4 wt% CES	S3
GGW with 8 wt% CES	S4
GGW with 4 wt% limestone	S5
GGW with 8 wt% limestone	S6
GGW with 4 wt% RES	S7
GGW with 8 wt% RES	S8
GGW with 4 wt% kaolin	S9
GGW with 8 wt% kaolin	S10
GGW with 4 wt% ADP	S11
GGW with 8 wt% ADP	S12
GGW with 4 wt% CES and 4 wt% ADP	S13

An additive to biomass ratio of 4% and 8% (w/w dry biomass mass basis) were tested for the samples of GGW after a thorough literature survey [7, 8, 11, 16] and considering the high ash content of the GGW sample under consideration.

Samples Preparation

To improve the uniformity and combustibility of the samples, the GGW samples were converted into pellets (1/2″ dia × 1″ L) using a portable Parr 2811 pellet hand press before sintering experiments. For the additive-based runs, firstly, finely powdered additives and samples were manually mixed using a spatula for 10 min, and then they were homogenised using a mixer for 20 min before subsequently being pelletised for sintering tests. The thirteen samples prepared for biomass combustion based sintering experiments are listed in Table 1.

Apparatus Set-up and Experimental Procedure for Sintering Tests

In this work, combustion experiments were done under a fume cupboard by setting up a fixed-bed combustion system, as shown in Fig. 1 below. Both the apparatus set-up and the experimental procedure were adopted with slight modifications from similar previous studies [8, 17–19]. Despite the significant difference between the design and reaction dynamics of the laboratory-scale and commercial scale-thermochemical systems, lab-scale sintering evaluation of biomass feedstocks has been proven to be sufficiently helpful in predicting and fixing possible operational problems in the former [20].

In contrast to previous studies that just used oxidative media for combustion-based sintering trials, the reaction gas

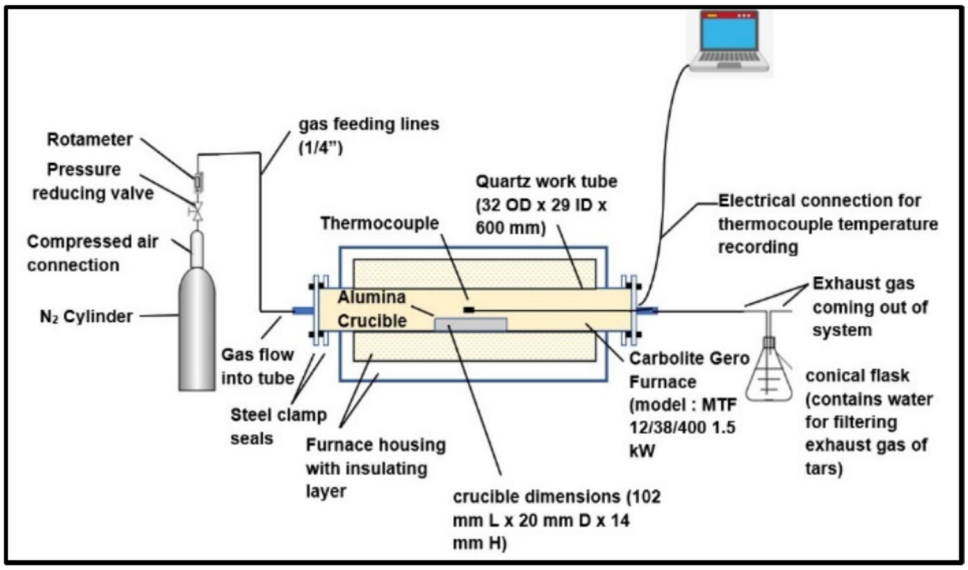

Fig. 1 Schematic diagram of laboratory tube furnace-based combustion experiment system

was switched to air from an inert (nitrogen) atmosphere at 700 °C. This was to simulate the conditions of the ash transformation reactions that occur during gasification [3] and combustion [21] processes during which biomass particles are subjected to both reducing and oxidative environments. Minerals transformation of biomass ash under pyrolyzing and oxidising atmospheres can differ considerably so splitting the reaction span into two gaseous regimes would affect the ash transformation mechanism [22]. Biomass particles, particularly in gasifiers, are exposed to oxidative media (such as air) after the regime of pyrolysis reactions ($\leq$700 °C) and experience temperatures as high as 1000 + /− 100 °C (or up to 1100 °C) due to exothermic reactions [9, 10]. In this temperature range of 700–1000 °C, inorganic/non-combustible components of biomass particles (i.e., ash) tend to melt or sinter in both gasification and combustion systems due to the formation of low-melting phases through various ash transformation mechanisms.

Procedure of Combustion Experiments

After the experimental station (Fig. 1) was set up, the GGW samples (i.e., S1–S13 as listed in Table 1) were combusted according to the following procedure.

1. 6–8 g of pelletised sample were placed in an open-top alumina crucible which was then placed in the middle of the furnace using a depth measuring tool to ensure even sample heating.
2. The ends of the work tube were then sealed by insulating plugs and thermocouple embedded steel clamps.
3. Nitrogen was purged through the system for 15 min at 0.5 L/min at ambient laboratory conditions before turning on the furnace heating. It was made sure that gas bubbles were continuously escaping through the surface of the water in the conical flask to confirm the system was leakproof.
4. Under the continuous flow of nitrogen, the furnace temperature was steadily increased to 700 °C, at which point the gas was switched to air.
5. The furnace temperature was further increased and maintained for 1 h at 1100 °C under continuous airflow to ensure the biomass sample was combusted entirely.
6. After the one-hour temperature hold-up experiment was terminated, the system was cooled down to approximately 400 °C while continuously flushing with air. The insulating plugs and steel clamp seals were removed from the work tube ends to aid in faster system cooling.
7. Once the system temperature dropped below 100 °C, the reaction crucible was removed from the furnace and left to cool naturally to laboratory conditions.
8. Biomass ash in the alumina crucible was visually analysed for sintering (as detailed in the next "Visual Evaluation of Sintering Tendency of Crude and Additive Modulated Mixtures of GGW" section) before being stored in a desiccator for further analysis.
9. Each experiment was repeated at least once for reliability purposes, and all results were found to be comparable in each set of experiments.

Analysis

Physiochemical Characterisation of GGW

The carbon, hydrogen, nitrogen, and oxygen contents of GGW (i.e. ultimate analysis (UA)) were determined by OEA labs Ltd, UK. The thermo-gravimetric analyser (TGA) of TA-Instruments (TGA 550) was used to carry out proximate analysis (PA) of a representative sample of GGW. It provided the percentage of moisture, volatile matter, ash, and fixed carbon content (by difference) in the original weight of the fuel. The results of these measurements have been listed in Table 2.

Visual Analysis of Sintering of Combusted Residues

The relative degree of biomass ash fusion or sintering of the combustion residues was assessed by visual observation and manual application of force (through hand and spatula). They were classified on a relative hardness scale of 1–5 according to the following graded scale, which, though not a standardized procedure, has been used in many previous studies with similar research goals [7, 8, 16, 23]: (1) Particles that did not show any signs of melting and were loose or easily crumbled on touch (2) somewhat sintered ash that retained a porous, brittle structure (3) partially melted hard sintered ash structure that required some force to be broken down (4) very hard slags and sintered ash structures that were impossible to break (5) completely melted ash that was stuck to the bottom of the crucible and could not be wholly scratched off.

Analytical Techniques Used for Analysis of Combustion Residues

Scanning Electron Microscopy (SEM, Model LEO 1455 VP) coupled with an Energy Dispersive Spectrometer (EDX, Oxford Instruments INCA-act) in the backscattered imaging mode has been used to determine all types of analysis of the elemental composition of GGW samples due to its suitability for the kind of work conducted and ease of operation. XRD (powder X-ray diffraction, Bruker Instrument Co., Ltd, Advanced D8) has been used to detect crystalline compounds present in biomass ash samples. These techniques

Table 2 Chemical characterisation of organic streams used

	Garden grass waste	Raw eggshells
Proximate analysis (wt%) (dry basis)		
Moisture	3.19	0.787
Volatiles	65.33	46.7885
Fixed carbon	9.52	0.017
Ash	21.97	52.405
HHV (MJ/kg)	14.7	–
Ultimate analysis (wt%) (dry basis)		
Carbon	35.75	17.01
Hydrogen	5.1	0.48
Oxygen	32.07	30.11
Nitrogen	2.84	–
Sulphur	0.31	–
Chlorine	0.97	–
Ash composition at 550 °C (wt%)		
Na	2.11	–
Mg	2.33	0.775
Al	3.22	0.91
Si	36.72	–
P	5.14	–
S	2.83	0.16
Cl	7.4	–
K	19.78	0.39
Fe	7.18	–
Ca	11.88	97.77
Ti	0.27	–
Cr	0.68	–
Mn	0.51	–

have been widely used to analyse combusted biomass ash residues from sintering tests to gain an in-depth insight into the reaction properties of different biomasses from a microscopic perspective [8, 17, 18]. The data acquired is used to elucidate the possible ash transformation mechanisms underlying the anti-sintering effects of the different additives in high-temperature reactors.

Ash Sample Preparation for SEM–EDX Analysis Samples were prepared differently for each type of analysis required from the SEM–EDX technique. To determine the semi-quantitative composition of the residues of sintering tests, ash samples were ground into a fine powder and a minute amount of sample was spread on a carbon tape sticking to specimen stubs and analysed at a magnification of 100×. However, to study the surface features of sintered ash, specimens were carefully taken from the top layer of combustion residues and analysed as such without any sample preparation (such as grinding). Different magnifications (up to 5000×) were used to explore the combustion residues' surface features, such as surface melting and cross-linked structure.

The elemental distribution and correlation of the most dominant elements present in the combustion residues structure were examined by obtaining elemental maps at the magnification of 5000×. Spot analysis of the sites of significant interest in the elemental maps was carried out. The acquired data was used in conjunction with the XRD diffractograms to estimate better the crystalline and amorphous compounds present in the ash structure.

Parameters for XRD Analysis of Ash Since the ash cooling history affects the crystallisation process [23], it was ensured that all combusted biomass residues were cooled under similar conditions so the XRD results would be comparable. For XRD-analysis, samples of residues from the sintering tests were finely ground before diffractograms were recorded on a Brucker D8 Advance diffractometer (cathode Cu, $K\alpha1 = 1.5418$ Å, 10–90°, detector opens at 2.425°, step 0.00205°, time per scan = 0.2 (s), 40 kV, 25 mA, div split 0.6). The crystalline phase analysis was performed with DIFFRAC plus EVA using the ICDD (International Centre for Diffraction Data) database. The semi-quantitative analysis of crystalline phases was performed by the normalised reference intensity ratio (RIR) method, whose precision is estimated as ± 10% and ± 25% for strongly diffracting phases and weakly diffracting phases, respectively [24].

Results and Discussion

Chemical Characterisation of Garden Grass Waste and Additives

The chemical characterisation (PA, UA and high-temperature ash composition) of the crude GGW and eggshells waste is presented in Table 2 [25]. The overall chemical composition of GGW used in this study seems to agree reasonably well with the previous studies (as shown in Table 3) [3, 4, 26] but with a dramatically higher ash content of 22 wt% of dry fuel and rather higher Fe and Al contents. The biomass ash composition data in oxides form from the literature has been converted into elemental wt% basis and normalised for analysis against the results of this study (Table 3). The calorific value of GGW was also found acceptable for the energy valorisation process.

Table 3 Proximate and ultimate analysis of garden waste from literature

	From this study	Results from published literature		
		3.9	4.25	26.27
Proximate analysis wt%				
Moisture	3.19	9.23	10	5.4
Volatiles	65.33	64.21	67.1	63.42
Fixed carbon	9.52	16.6	18.4	17.48
Ash	21.97	9.96	14.5	13.7
Ultimate analysis wt% (dry basis)				
C	35.75	42.5	38	34.25
H	5.1	6.4	4.4	3.22
O	32.07	39.83	42	47.31
N	2.84	1.3	1.1	1.1
S	0.31	< 0.01	–	0.42
Cl	0.97	–	–	–
Ash composition wt%				
Na	2.11	0.03–2.3	0.29	0.61
Mg	2.33	0.85–5.18	2.81	4.74
Al	3.22	0.17–0.67	1.15	0.81
Si	36.72	4.07–39.63	79.63	39.99
P	5.14	–	2.84	4.03
S	2.83	0.33–3.95	1.45	–
Cl	7.4	–	0.6	–
K	19.78	1.22–22.15	4.96	29.18
Fe	7.18	0.20–0.60	1.27	0.56
Ca	11.88	2.13–31.66	5.01	20.012
Ti	0.27	–	–	0.1
Cr	0.68	–	–	–
Mn	0.51	–	–	–

Visual Evaluation of Sintering Tendency of Crude and Additive Modulated Mixtures of GGW

As expected from the initial fuel analysis and the high-temperature ash (HTA) (i.e., ash that is prepared at the temperature of 550 °C) composition of GGW (Table 2), the ash residues of crude GGW (S1) were entirely fused and molten. They were impossible to scratch off completely from the bottom of the test crucible. Some of the ash particles were stuck to the crucible as greenish glass-like bubbles, indicating that the ash melted to the liquid phase and acquired a glassy appearance on cooling [23]. This finding was consistent with the already published results of Siddiqui et al. [3] who reported the severe melting and clinkering tendency of garden grass waste ash at high grate temperatures inside a downdraft gasifier [27].

On the other hand, the ash residues of GGW samples that were doped with 4 wt% lime (S2) and 4 wt% CES (S3) were substantially less melted, and they were not stuck to the crucible bottom. However, they were hard, indicating their tendency to make viscous melts, agglomerates and clinkers in high-temperature thermochemical systems. Positively, the ash residues of both S2 and S3 were observed to be equally sintered, which suggested that CES and commercial lime can be used interchangeably as a calcium-based anti-sintering additive to enhance biomass fuel melting characteristics.

The ash residues of S4 (a mixture of GGW and 8 wt% CES) were soft and crumbled on touch and indicated no signs of melting.

A similar partial reduction in the sintering of GGW ash contents was observed with substantially hard ash residues upon the addition of limestone (S5), raw eggshells (S7), kaolin (S9) and ADP (S11) in 4 wt% proportion. In contrast, the inclusion of these additives in 8 wt% proportion completely inhibited the melting of ash residues of S6, S8, S10, and S12, with no visual signs of sintering.

The difference between the anti-sintering performance of RES and limestone was negligible, with the ash of samples modulated with RES slightly more friable than the ones containing limestone.

Though simultaneous mixing of both calcium (CES) and phosphorous (ADP)-based additives in 4 wt% proportion each significantly reduced the ash melting of GGW (in S13), the results were less pronounced than those

modulated with respective single additive streams (S4 and S12) comprising 8 wt% of Ca or P contents alone.

The surface of the combustion residues of GGW pellets that contained calcium-based additives was swollen, with holes indicating the release of gases (possibly CO_2). In contrast, the surface of the pellets containing phosphorous and kaolin-based additives was shrunken. Similar relevant studies have ascribed such shrinking and swelling behaviour to the different reaction chemistry triggered in each case [19, 23]. Ash residues of S13, which contained both Ca and P-based additives, were swollen.

Notably, the combustion residues of GGW containing 8 wt% of kaolin (S10) were the softest compared to the fuel containing 8 wt% of other additives (i.e., S4, S6, S8 and S12).

The relative anti-sintering performance of additive modulated mixtures of GGW is summarised as follows in order of reducing ash softness or effectiveness when classified on a hardness scale of 1–5 (according to the procedure mentioned in "Visual Analysis of Sintering of Combusted Residues" section, Fig. 2).

8 wt% Kaolin (S10) > 8 wt% CES (S4) > 8 wt% ADP (S12) > 8 wt% RES (S8) > 4 wt% CES and 4 wt% ADP (S13) > 8 wt% LS (S6) > 4 wt% Kaolin (S9) > 4 wt% CaO (S2)/4 wt% CES (S3) > 4 wt% ADP (S11) > 4 wt% RES (S7) > 4 wt% LS (S5) > Raw GGW (S1)

Since the relative performance of the sintering evaluations of the test mixtures was based on visual observations, the results may be considered subjective [8, 17, 18]. However, lab-scale combustion experiments were repeated twice, and no variations in the slagging tendency of the samples could be determined between the replicates.

Study of Possible Sintering and Anti-Sintering Mechanisms of Crude and Additive Modulated Samples

Underlying Reasons for Melting Characteristics of Crude GGW

To understand the underlying reason for the severe melting of the GGW ash residues, the ash composition of the crude GGW (containing Si (36.72%), K (19.78%), Ca (11.88%), Cl (7.4%), Fe (7.18%) and P (5.14%)) is compared with high-quality reference woody biomass and other low melting herbaceous biomass streams [28, 29] in the compositional ternary phase diagram (Fig. 3) by normalising the ash composition data in the Excel sheet according to the new classification system suggested by Vassilev et al. [29] for the comparison of IDT (initial deformation temperature) of ash which indicates the clinker formation tendency of the crude biomass species (Table 4). Figure 3 suggests that the melting and mineral transformation behaviour of the GGW ash would be similar to other herbaceous biomass streams. Thus, the phenomenon explaining their ash transformation mechanisms in high-temperature thermochemical systems would also apply to GGW [28, 29].

Crystalline Phases in Combustion Residues of GGW XRD analysis of the ash residues of crude GGW (S1) combusted at 1100 °C detected the presence of quartz, cristobalite, micro-

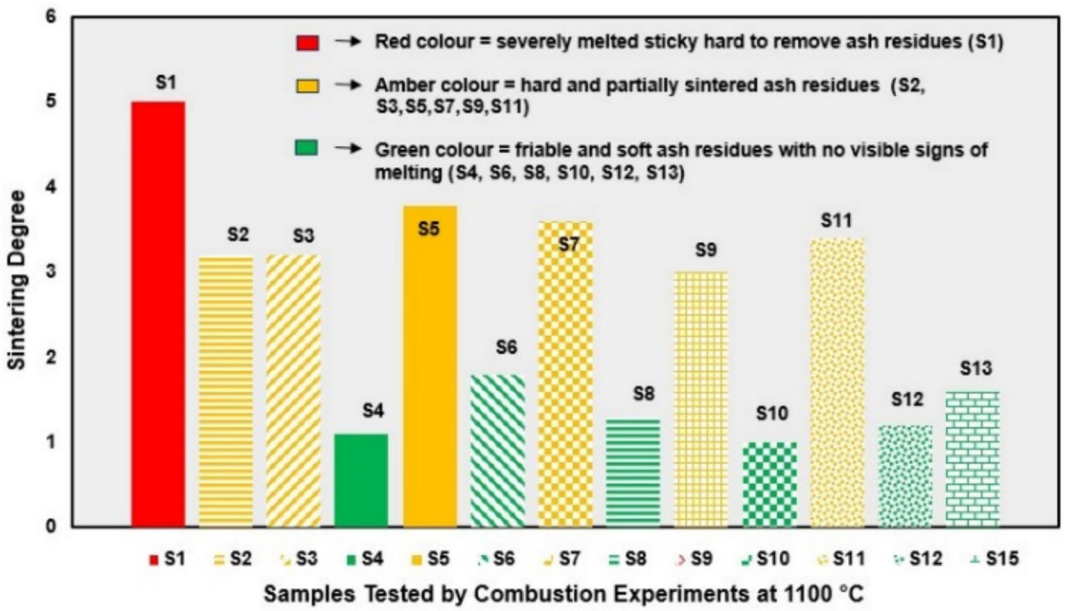

Fig. 2 Relative impact of different additives and their proportions on the sintering degree of garden grass waste

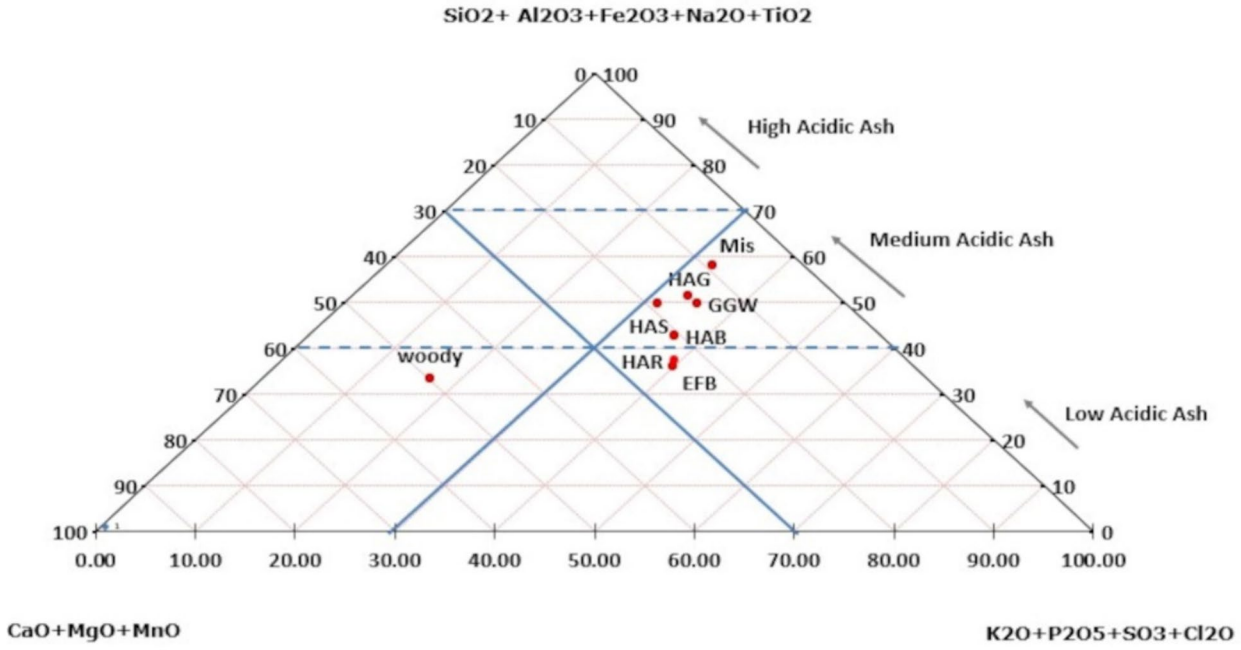

Fig. 3 Relevant positions of high temperature ash composition of different non-woody biomass streams and woody biomass in the chemical classification system of biomass ash, wt% [28, 29]. Mis Miscanthus, EFB empty fruit bunch, HAB Herbaceous and agricultural biomass, HAG Herbaceous and agricultural grass, HAR Herbaceous and agricultural residues, HAS Herbaceous and agricultural straws, Woody woody biomass; and GGW Garden grass waste from this work

cline ($KAlSi_3O_8$), Fe-diopside ($(Ca_{0.92}Fe_{0.08})(Fe_{0.16}Mg_{0.84})(Si_2O_6)$), and Fe-whitlockite ($((Ca_{18.07}(Mg_{1.83}Fe_{0.17})(PO_4)_{12.14}(PO_3(OH))_{1.86})$) in large amounts with trace amounts of magnesium aluminium silicate and maghemite-C (Table 5). This confirmed that, like other herbaceous biomass, the ash residues of GGW (S1) melted severely due to the formation of complex miscible mixtures of low-melting silicates and phosphates. Microcline (base formula $KAlSi_3O_8$), diopside (base formula $CaMg(SiO_3)_2$) and whitlockite (base formula $(Ca_{2.71}Mg_{0.29}(PO_4)_2)$ have widely been observed in the melted residues of Si-rich agricultural and herbaceous biomass fuels [9, 10, 30–32]. Their low melting eutectics formation tendencies have been attributed to the severe slagging in biomass ash [30, 31]. Considering the chemical composition of GGW ash, microcline and diopside possibly formed due to the following reactions [31].

$$K_2SO_4 + Al_2O_3 \cdot SiO_2 + 5SiO_2 \rightarrow 2KAlSi_3O_8(\text{Microcline}) + SO_3 \quad \text{(R1)}$$

or

$$2KCl + Al_2O_3 \cdot SiO_2 + 5SiO_2 + H_2O \rightarrow 2KAlSi_3O_8(\text{Microcline}) + 2HCl \quad \text{(R2)}$$

$$Ca_2SiO_4 + 2MgO + 3SiO_2 \rightarrow 2CaMgSi_2O_6(\text{Diopside}) \quad \text{(R3)}$$

or

$$CaSiO_3 + MgO + SiO_2 \rightarrow CaMgSi_2O_6(\text{Diopside}) \quad \text{(R4)}$$

Higher ratios of Si/K through soil contamination of herbaceous biomass streams (such as crude GGW as evidenced in Table 1) have widely been known as an underlying reason for intensifying the ash melting of combusted ash residues [9, 10].

Higher concentrations of Fe present in the GGW seemed to have facilitated the cation exchange in the crystal lattice of diopside (generating Fe-diopside) and whitlockite (generating Fe-whitlockite), lowering their melting points as compared to their pure compounds [33, 34]. Such variations of crystalline structures by cationic modifiers in silicates (such as Fe- diopside) [18] and phosphates (such as Fe-whitlockite) have also been observed in previous studies [18, 32].

Silica has also often been identified in the form of quartz and cristobalite in severely melted herbaceous biomass streams [8–10, 18, 32] that also contain low melting silicates, and we can reasonably describe the unremovable sticky nature of the severely melted residues of GGW (as observed during the sintering evaluation results in "Visual Evaluation of Sintering Tendency of Crude and Additive Modulated Mixtures of GGW" section) to the uncombined SiO_2 and Fe-compounds which are reported to increase the viscosity of the K-feldspars melt system [35, 36].

Table 4 Ash composition of samples combusted at 1100 °C

Ash COMPOSITION (wt%)													
Additive type	No additive	4 wt% CaO	4 wt% CES	8 wt% CES	4 wt% LS	8 wt% LS	4 wt% RES	8 wt% RES	4 wt% Kaolin	8 wt% Kaolin	4 wt% ADP	8 wt% ADP	CES 4 wt% + ADP 4 wt%
Sample #	S1	S2	S3	S4	S5	S6	S7	S8	S9	S10	S11	S12	S13
Na	1.68	1.2	1.45	0.84	1.49	1.26	1.26	1.08	1.4	1.35	1.59	1.69	1.57
Mg	2.08	1.69	1.81	1.65	1.68	1.63	1.94	1.81	1.77	1.57	2.11	1.68	1.65
Al	4.63	3.19	3.64	2.46	4.06	3.4	3.7	3.23	9.71	14.98	3.93	3.45	3.24
Si	54.64	38.9	39.14	26.81	43.25	33.62	40.77	35.52	47.35	45.875	46.35	43.42	31.55
P	4.46	3.98	4.99	3.19	4.05	3.91	4.15	4.02	4.29	3.855	15.02	18.71	14.18
S	nd	0.46	1.73	3.4	0.83	1.61	1.5	2.29	0.59	nd	nd	0.25	1.82
Cl	0.19	0.31	0.28	0.2	0.37	0.86	0.45	0.13	0.27	nd	nd	nd	0.68
K	12.35	7.84	7.54	3.82	9.89	7.53	9.05	6.57	15.69	14.11	11.98	13.13	6.85
Ca	10.08	35.71	33.63	52.97	26.22	40.38	29.49	39.99	10.63	9.59	10.2	8.17	31.635
Ti	0.25	0.06	nd	nd	nd	nd	nd	nd	0.59	0.725	0.21	0.13	nd
Cr	0.88	0.66	0.43	0.62	1.37	0.63	0.58	0.41	0.68	0.575	0.78	1.34	0.815
Mn	0.3	0.08	nd	nd	0.46	0.19	nd	nd	0.6	0.25	nd	0.16	nd
Fe	8.53	5.92	5.35	4.09	6.05	5.02	7.17	4.97	6.46	6.715	7.86	7.9	5.56
Ni	nd	nd	nd	nd	nd	nd	nd	nd	nd	nd	nd	nd	0.46
Cu	nd	nd	nd	nd	nd	nd	nd	nd	nd	0.405	nd	nd	nd

nd not detected able 7

Table 5 Crystalline Phases Identified in Ash Residues of Samples Combusted by XRD Analysis (wt%)

Additive type		Non-additive	Ca-based additives							Al-based additive		P-based additive		Mixed stream
Tab			4 wt% CaO	4 wt% CES	8 wt% CES	4 wt% LS	8 wt% LS	4 wt% RES	8 wt% RES	4 wt% Kaolin	8 wt% Kaolin	4 wt% ADP	8 wt% ADP	CES 4 wt% + ADP 4 wt%
Crystalline phases	Melting Point °C	S1	S2	S3	S4	S5	S6	S7	S8	S9	S10	S11	S12	S13
Quartz, syn (SiO2)	1713	√	√	√	√	√	√	√	√	√	√	√	√	√
Cristobalite, syn (SiO2)	1705	√	√	√	√	√	√	√	√	√	√	√	√	√
Magnesium Aluminium Silicate (Mg2Al4Si5O18)	900	√												
Microcline, sodian (K.5Na.5AlSi3O8)	1170	√						√						
Microcline, sodian (K.5Na.5AlSi3O8)	1170	√						√						
Diopside (Ca0.92Fe0.08) (Fe0.16Mg0.84)(Si2O6)		√	√	√										
Diopside, syn Ca0.964 Mg(Si2O6)	1392									√				
Calcium Magnesium Iron Silicate (Mg0.998 Fe0.002) (Ca0.956 Fe0.044) (Si2O6)						√	√	√	√					
Augite (Mg0.74 Fe0.21 Al0.04 Ti0.01) (Ca0.78 Na0.02 Mg0.03 Fe0.16 Mn0.01) (Si1.94 Al0.06 O6)			√											
Majorite (Ca-bearing) syn, Calcium Magnesium Silicon Silicate (Ca0.49Mg2.51)(MgSi) (SiO4)3												√		
Pseudowollastonite Ca3(Si3O9)			√	√										√
Pseudowollastonite,syn (CaSiO3)				√				√				√		
Wollastonite-1A, manganoan (Mn0.12Ca2.88) (SiO3)3			√	√		√								
Wollastonite-2 M (CaSiO3)							√		√					
Wollastonite (Ca0.957Fe0.043 O3Si)					√									√
Calcium Silicate (CaSiO3)	~1540–1544				√									
Gehlenite (Ca1.96 Na.05) (Mg.24 Al.64 Fe.12) (Si1.39Al.61O7)			√	√			√	√	√					
(Gehlenite, magnesian, siliceous, syn) Ca2 (Al0.65 Mg0.35)((Al0.65 Si1.35) O7)					√									
Calcium Aluminum Silicate (CaAl2Si2O8)	~1554–1590					√		√						

Table 5 (continued)

Additive type		Non-additive	Ca-based additives							Al-based additive		P-based additive		Mixed stream
Tab			4 wt% CaO	4 wt% CES	8 wt% CES	4 wt% LS	8 wt% LS	4 wt% RES	8 wt% RES	4 wt% Kaolin	8 wt% Kaolin	4 wt% ADP	8 wt% ADP	CES 4 wt% + ADP 4 wt%
Crystalline phases	Melting Point °C	S1	S2	S3	S4	S5	S6	S7	S8	S9	S10	S11	S12	S13
Calcium dialuminate (Ca(Al2O4))	1604							√						
Potassium Calcium Silicate (K4CaSi3O9)			√	√	√	√		√	√					√
Potassium Aluminum Silicate (KAlSiO4)	1684–1750									√				
Jadeite (NaAlSi2O6)	1118–1553									√				
Leucite, syn (KAlSi2O6)	1686									√	√			
Anorthite, sodian, ordered ((Ca,Na) (Al,Si)2Si2O8)	1553										√			
Potassium Aluminum Silicate (K(AlSi3O8))	1170										√			
Potassium tecto-alumotri silicate | Potassium Aluminum Silicate (K0.95(AlSi3O8))											√			
Anhydrite, syn (CaSO4)	1450			√	√	√	√	√	√					
Dipotassium dicalcium sulfate(VI) | Potassium Calcium Sulfate) (K2Ca2(SO4)3)							√	√	√					
Calcite (Ca(CO3))	1339						√							
Lime (CaO)	2570–2597				√				√					
Maghemite-C, syn (Fe2O3)		√												
Hematite (Fe2O3)	1566										√			
Potassium Iron Oxide (KFeO2)	> 1135		√	√										
Aluminum phosphate(V) | Aluminum Phosphate) (Al (PO4))	2000												√	
Potassium Calcium Magnesium Phosphate (Ca9MgK(PO4)7)													√	√
Hydroxylapatite, syn (Ca10(PO4)5.55(HPO4)0.45(O0.53(OH)1.39))	1400		√	√										√
Calcium Hydrogen Phosphate Hydrate (Ca8H2(PO4)6 ·5H2O)														√
Whitlockite, syn (Ca18.07(Mg1.83Fe0.17) (PO4)12.14(PO3(OH))1.86)	1400	√												

Table 5 (continued)

Additive type		Non-additive	Ca-based additives								Al-based additive		P-based additive		Mixed stream
Tab			4 wt% CaO	4 wt% CES	8 wt% CES	4 wt% LS	8 wt% LS	4 wt% RES	8 wt% RES		4 wt% Kaolin	8 wt% Kaolin	4 wt% ADP	8 wt% ADP	CES 4 wt% + ADP 4 wt%
Crystalline phases	Melting Point °C	S1	S2	S3	S4	S5	S6	S7	S8		S9	S10	S11	S12	S13
Whitlockite, syn (Ca2.71Mg0.29(PO4)2)													√		
Calcium Hydrogen Phosphate Hydroxide (Ca9HPO4(PO4)5OH)					√	√		√	√						
Apatite A (Ca10(PO4)6((CO3)0.75(OH)0.5))	1270–1660						√								
Potassium Calcium Iron Phosphate (KCaFe(PO4)2)											√	√	√	√	√
Calcium Iron Phosphate Hydroxide Hydrate (CaFe5(PO4)5(OH)(H2O))														√	

Surface Morphology of Crude GGW Ash Residues The morphology and microchemistry data of the severely melted ash residues of crude GGW (S1) at a magnification of 5000× is shown in Fig. 4. Aggregates of fused ash particles of different sizes embedded in a dominantly large smooth continuous region are clear (Fig. 4a). It indicates the co-presence of crystalline phases with the amorphous phases [18, 19], which was in agreement with the results of the visual analysis of the sintering degree ("Visual Evaluation of Sintering Tendency of Crude and Additive Modulated Mixtures of GGW" section). EDX-based elemental mapping of the scanned cross-sectional area of ash residues showed strong overlapping between the K-Al-Si and K-Ca-P regions (Fig. 4), confirming the co-existence of low- melting eutectic mixtures of phosphates and silicates (which mainly contained microcline, diopside, and whitlockite as predicted by HTA of GGW and identified by XRD analysis). In addition, the presence of pure low-melting Fe-silicates (spot 5 in Fig. 4a with Fe 24.08% and Si 56.89%), and albite (or its modifiers by the presence of Na in all EdX spots in Fig. 4) in the amorphous melted fraction of ash can be indirectly deduced as they were not detected in XRD analysis. The elemental map of Si appeared the most dense (with Si identified as the most dominant element in all the EDX spots in Fig. 4 except spot 2), eluded to the presence of free unreacted silica as determined by XRD phase analysis through the presence of quartz and cristobalite (Table 5) while the elemental map of Fe appeared mainly lean showing iron particles scattered all around in between regions occupied by different elements confirming the role it played in lowering the melting point of the eutectic mixtures of silicates and phosphates (by acting as a cationic modifier and facilitating Fe-eutectic mixtures) and thereby heavily melting the ash contents of GGW (S1).

It is rare for Cl not to have evaporated out of the biomass ash system well below 1100 °C [9, 10]. So, the presence of Cl in the scanned area of the S1 ash residues suggests the presence of amorphous melted alkali-chlorides or organic-bound chlorine in the unburnt carbon matrix that was unable to oxidise due to the blanketing effect of the melted phases [19]. For this reason, NaCl has also been identified in biomass ash samples subjected to temperatures as high as 1100 °C in similar relevant studies [37]. It is noteworthy that elements which are present in trace amounts (such as Cl, Ti, Cr etc.) would be more likely to be only identified at the localised positions through the EDX spot analysis and would be invisible in the overall composition of the sample due to being beyond the detection limit [7, 23]. Crystalline compounds of such elements would also be invisible in an XRD diffractogram as they would fail to generate the sufficient response required for detection with certainty. The characteristic ash melting features of GGW are shown in Fig. 5 below.

Anti-sintering Effects of Ca-Based Additives on GGW

It is clear from the ternary diagram (Fig. 6), which was plotted in Excel by using the normalised ash composition data of the samples of this study and from published literature [23, 38] that the low-melting GGW ash was more Si-rich and Ca-deficient. As the proportion of the Ca was increased through the inclusion of 4 wt% additives, the composition of its ash became closer to the Ca-dominant end of the ternary diagram, shifting away from the earlier position that was closer to the SiO_2-high corner indicating the likelihood of formation of high melting Ca-silicates as suggested by previous studies [35]. Since CES was more or less compositionally the same as lime and RES to limestone, the composition of their subsequent ash residues was also observed to be approximately similar (Table 4). That is why the anti-sintering efficacy of CaO and CES was the same, and that of RES and LS was alike (Fig. 2). Ash residues of the GGW—8 wt% CES mixture (S4) which were observed to be the most friable among all the Ca-doped mixtures, acquired the closest position to the Ca-dominant end of the ternary diagram (with a CaO content of 63.36 wt%), indicating the likelihood of formation of Ca-rich compounds (such as Ca-silicates, $CaO/CaCO_3/Ca(OH)_2$). This zone is clearly located in the phase diagram region where high melting pure Ca-silicates appear (Fig. 6) [39]. A huge difference was observed in the positions of the data points representing the ash of the samples that were modified with 8 wt% of Ca-based additives and those which only contained 4 wt%. This supports the hypothesis that the partial reduction in the melting tendency of the S2, S3, S5, and S7 samples can be attributed to the lack of a sufficient amount of Ca required to completely consume the reactive silica to inhibit the formation of low melting K-silicates [23] altogether (and to facilitate the stripping of K-out of mixtures of melted K-silicates).

Results listed in Fig. 6 are similar to those reported by Liang [23, 38], who observed the elimination of ash melting of barley husk, rye straw and barley straw with the addition of Ca-rich additive (calcite). Since, as is clear from the ternary phase diagram (TPD) (Fig. 6), barley husk (with Si 47.31%, K 41.36%, Ca 11.33%) and barley straw (with Si 34.13%, K 41.75%, Ca 24.12%) ashes had lower Si contents than GGW (with Si 53.7%, K 28.93%, Ca 17.37%) the addition of only 4 wt% of calcite was sufficient for those feedstocks to entirely eliminate the melting of their ashes whereas 8 wt% of Ca-additives were required to completely inhibit the melting of GGW ash due to excessive contamination with mud (because the GGW sample was visibly muddy when collected) [23]. Relevant positions of ash composition of raw and additive modulated mixtures of GGW in the chemical classification system of biomass ash on a wt% basis have been shown in Fig. 7.

Composition of Crystalline Phases in Ca-doped Mixtures of GGW The results of XRD analysis for all Ca-doped samples confirmed the redistribution of Si from potassium silicates to calcium silicates with increasing Ca contents of the parent fuel (Table 5). High melting Ca-silicates/alumino-

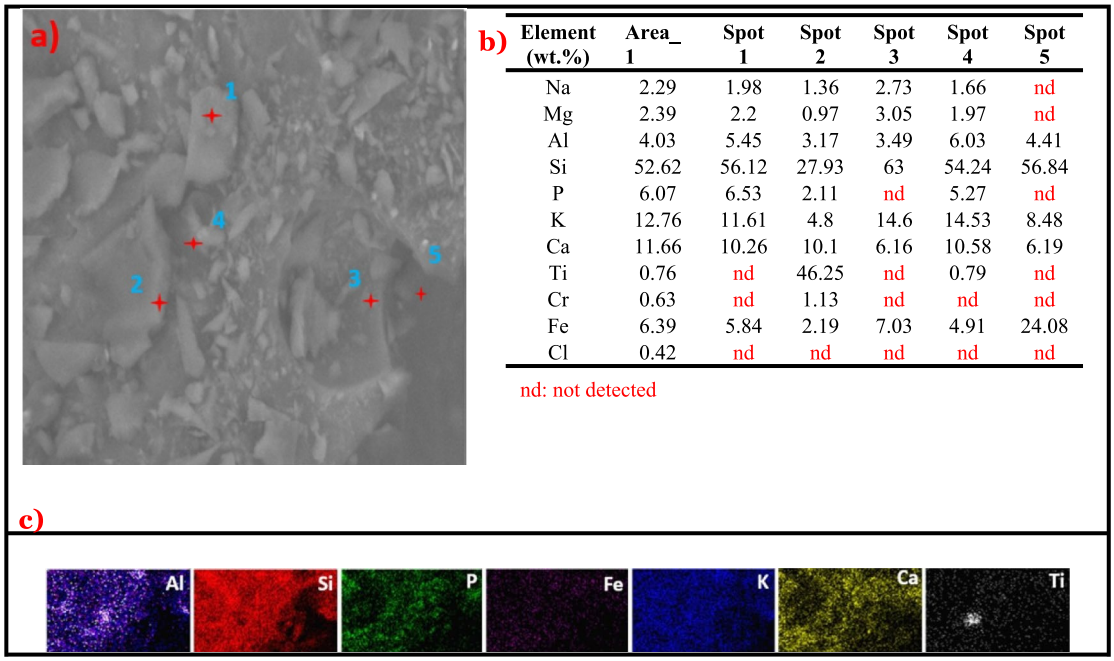

Element (wt.%)	Area_1	Spot 1	Spot 2	Spot 3	Spot 4	Spot 5
Na	2.29	1.98	1.36	2.73	1.66	nd
Mg	2.39	2.2	0.97	3.05	1.97	nd
Al	4.03	5.45	3.17	3.49	6.03	4.41
Si	52.62	56.12	27.93	63	54.24	56.84
P	6.07	6.53	2.11	nd	5.27	nd
K	12.76	11.61	4.8	14.6	14.53	8.48
Ca	11.66	10.26	10.1	6.16	10.58	6.19
Ti	0.76	nd	46.25	nd	0.79	nd
Cr	0.63	nd	1.13	nd	nd	nd
Fe	6.39	5.84	2.19	7.03	4.91	24.08
Cl	0.42	nd	nd	nd	nd	nd

nd: not detected

Fig. 4 **a** SEM micrograph of combusted residues of crude GGW at the magnification of 5000×, **b** average EDX composition of the overall cross-sectional area of the residues and the points of interest, **c** concentrational profile of the elemental maps

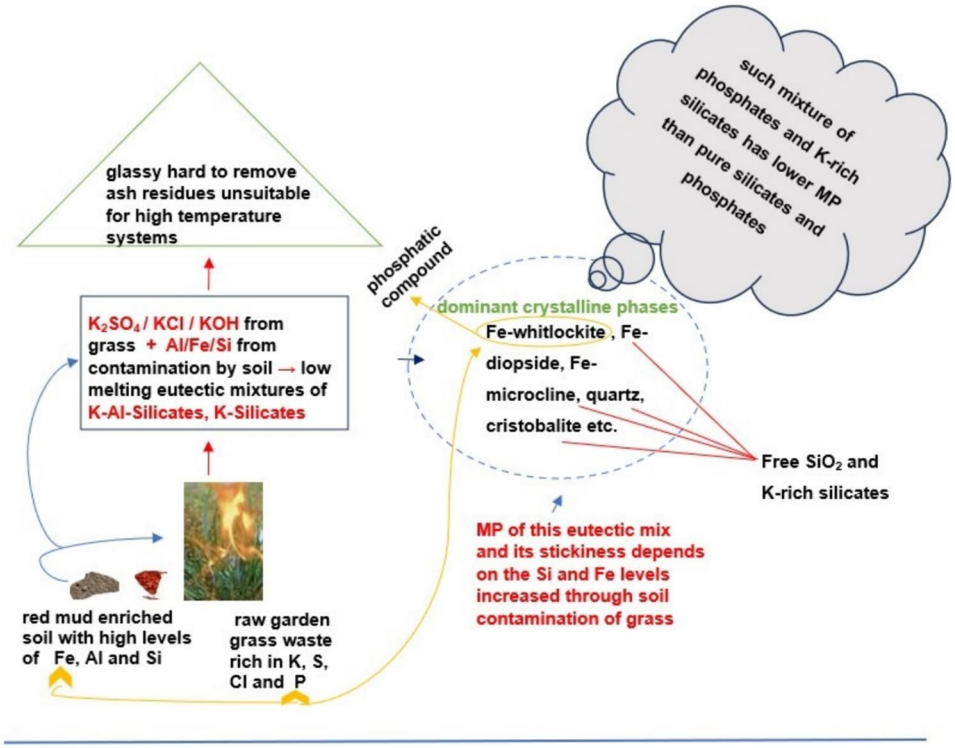

Fig. 5 Important features of melting characteristics of garden grass waste (GGW) ash

silicates (such as different crystalline modifications of pseudowollastonite, wollastonite, and gehlenite etc.) were identified in the partially melted ash of the samples that were doped with 4 wt% of Ca-based additives (S2, S3, S5, S7) but the formation of low-melting K-silicates was also indicated by the presence of small amounts of microcline, Ca-Mg-Fe-silicates and potassium calcium silicates (Table 5). On the contrary, no low melting eutectic forming silicates (such as microcline, sanidine, diopside, etc) were identified in the ash of the samples which were doped with 8 wt% of Ca-based streams (S4, S6, S8), and most Ca-silicates observed were pure compounds without any modifiers (such as cations of Fe, Al, Mg which lower the MP of compounds) which certainly contributed towards the enhancement of the melting characteristics of GGW ash making it more friable. This is because higher proportions of Ca in the ash of the samples S4, S6, and S8 facilitated the complete substitution of Al and Fe cations in Ca-silicates [40].

Upon addition of Ca-based additives to the GGW, the high melting Ca-rich phases possibly formed due to the following reactions [31].

$$CaO + xAlSi_yO_Z \rightarrow Ca - \text{aluminosilicates} \quad \text{(R5)}$$

$$Ca(OH)_{2(g)}/CaCO_{3(g)} + SiO_{2(s)} \rightarrow CaO.SiO_{2(s)} + H_2O/CO_2 \quad \text{(R6)}$$

Different high-melting Ca-silicates (such as gehlenite, wollastonite, pseudowollastonite etc.) were formed due to the varying proportions of Ca and Si in the GGW-additive mixtures which is a common trend reported in many similar studies [9, 10]. The higher share of these high-melting phases in combustion residues of Ca-dopped samples has been reported to decrease their sintering degree noticeably. In the residues of samples that contained 8 wt% of Ca-based additives, in addition to the pure-Ca-silicates, a surplus of unreacted Ca was also identified in the form of CaO (in ash residues of S4 and S8) and $CaCO_3$ (in the ash residues of S6) which due to their high melting refractory nature also helped in complete mitigation of the melting of GGW ash [23, 38]. Identification of $CaCO_3$ in 8 wt% LS is more likely an artefact of the experiment in which CaO is possibly converted to $CaCO_3$ by absorbing CO_2 during cooling [8].

A trace amount of potassium iron oxide (K_2FeO_4) was identified in the ash of the samples, which contained 4 wt% of CaO (S2) and 4 wt% of CES (S3). It can be reasonably assumed that it either formed due to the reaction between hematite present in the GGW ash and the gaseous K-species that were being stripped out of the ash melt system by the Ca-rich additives, or it could already present in dissolved form in an amorphous fraction of the severely melted ash residues of GGW (S1), and it only became visible in the XRD results when the ash melted amorphous fraction reduced on the enhancement of Ca-content in the fuel-additive mixture [31].

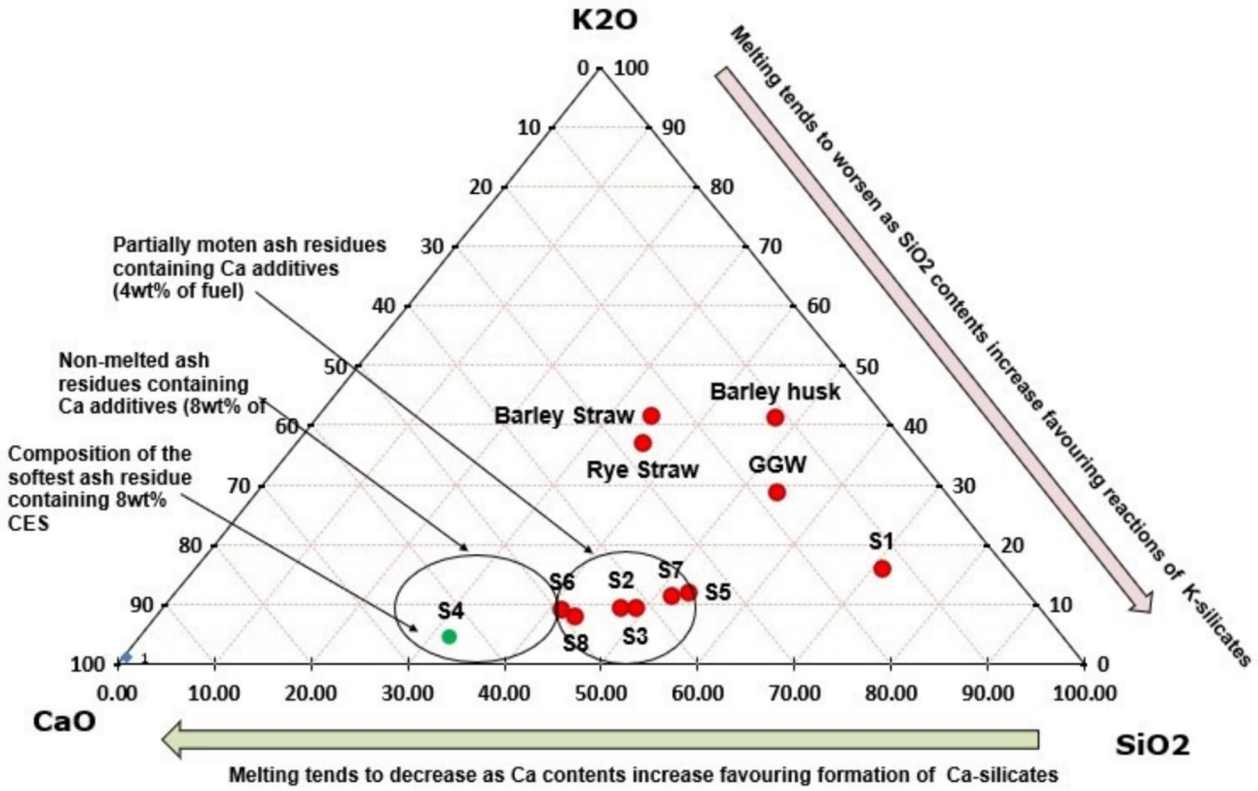

Fig. 6 Elemental composition of ash of different low-melting non-woody biomass streams, crude GGW of this study and its Ca-dopped mixtures in the ternary diagram of K2O-CaO-SiO2 system

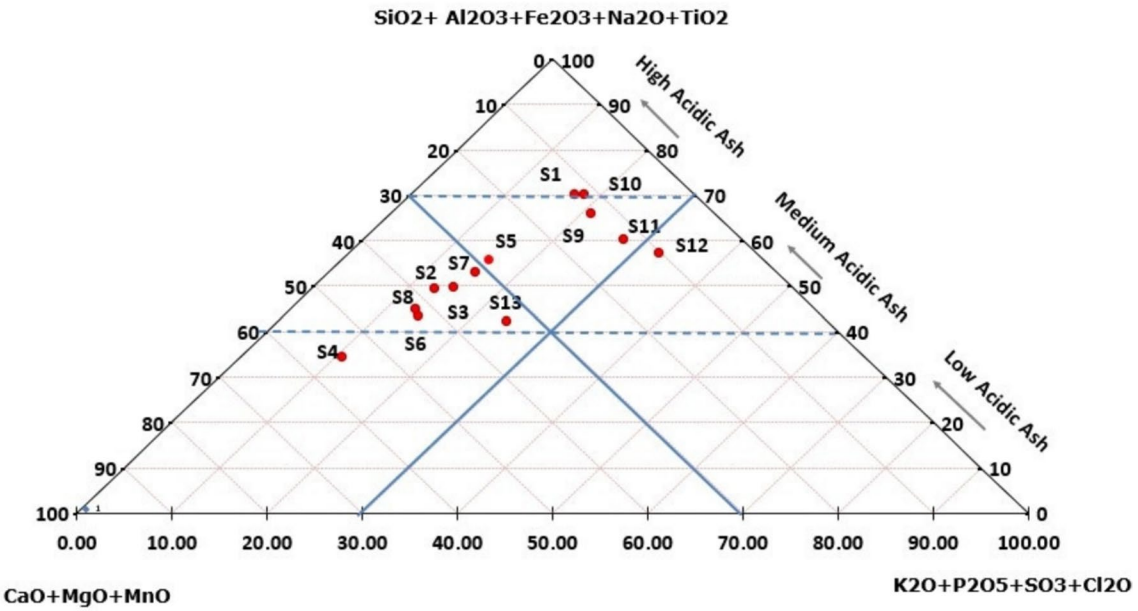

Fig. 7 Relevant positions of ash composition of raw and additive modulated mixtures of GGW in the chemical classification system of biomass ash, wt%

Anhydrite ($CaSO_4$) was also identified in all Ca-doped ash samples (except 4 wt% CaO-based sample S3, which possibly didn't generate a sufficient response to be picked up by XRD). It confirmed the absorption of SO_2 by the Ca-based additive streams, as also suggested by the identification of S contents in the overall chemical composition of Ca-doped samples (Table 5) and as reported by previous studies [8–11].

The formation of anhydrite $CaSO_4$ possibly occurred by the reaction of organic bound S of eggshells/GGW with the CaO over 800 °C temperature [9, 10].

$$CaO_{(s)} + SO_{2(g)} + \frac{1}{2}O_{2(g)} + CaSO_{4(s)} \quad \text{(R7)}$$

Trace amounts of S were also detected as $K_2Ca_2(SO_4)_3$ in XRD diffractograms of ash samples containing 8 wt% of LS (S6), 4 wt% of RES (S7) and 8 wt% of RES (S8). Such S-based crystalline phases of K and Ca have often been identified by other researchers in the ash samples of Ca-enriched biomass fuels [41–43].

Unlike S1 ash residues, whitlockite was not identified in any Ca-doped samples. Instead, P ended up as high melting Ca-phosphates (such as apatite and different modifications of its basic crystalline structure, as shown in Table 5). Like the severely melted ash residues of S1, quartz and cristobalite were also identified in the ashes of all Ca-doped samples. They seemed to have contributed to enhancing the ash melting characteristics of Ca-doped samples in S4, S6 and S8 in the absence of low melting K-silicates in particular.

Microchemistry and Surface Features of Ca-rich Combustion Residues The SEM images and results of EDX spot analyses of the ash residues of Ca-doped samples (S2–S8) are presented in Figs. 8, 9, 10, 11, 12, 13, 14 and the significant difference in their morphology is clear and affirm the varying melting characteristics of additive - modulated samples due to altered Ca/K ratio.

Overlapping elemental maps of Ca-P-K-Si clearly indicate the co-presence of Ca-silicates and Ca-rich phosphates in the ash of all Ca-doped samples (Figs. 8, 9, 10, 11, 12, 13, 14), which was in agreement with the identification of these phases by XRD analysis (Table 5). Elemental maps of Ca and S were also noticed to be overlapping in the EDX mapping of combustion residues of GGW samples that were doped with 8 wt% CES (Fig. 10c of S4), 8 wt% LS (S6, Fig. 12c), 4 wt% RES (S7, (Fig. 13c), and 8 wt% RES (S8, Fig. 14c), confirming the sorption of S by Ca-additives and the consequential formation of $CaSO_4$ as detected by XRD analysis and supported by significantly higher contents of Ca and S at EDX spot 5 of Figs. 10, 12, 14 and spots 2 and 4 in Figs. 13 and 14 respectively. Relatively smaller amounts of S in S2, S3, and S5 (Table 5) due to insufficient amounts of Ca-doping (i.e., 4 wt%) can be ascribed to the lack of high localised concentration of S particles (in Figs. 8, 9, and 11). Furthermore, Ca was identified as the most abundant element in most of the spots scanned by SEM–EDX (Figs. 10, 12, 14) in the samples containing 8 wt% of Ca-based additives (S4, S6, S8), indicating the presence of unreacted and surplus Ca as supported by XRD analysis (which identified trace amounts of CaO and $CaCO_3$).

Detection of significantly higher localised concentrations of Fe at some of the scanned EDX spots of Ca-doped ash residues indicated the presence of moderate contents of Fe rich-compounds such as Fe-silicates and Ca-Fe-silicates (as supported by EDX spots 1 and 2 in Fig. 8, spot 4 in Fig. 9, spot 5 of Fig. 10 spots 2 and 5 in Fig. 11, spot 2 in Fig. 12, spots 2 and 3 in Fig. 14). Some of these phases most likely have not been identified by XRD analysis, and we can deduce that either they were present in an amorphous form in the melt in the samples containing 4 wt% of Ca-based additives or they were unable to generate an adequate response in the XRD diffractogram due to their trace amounts [7, 23]. The characteristic ash melting features of Ca-dopped GGW samples are shown in Fig. 15.

Effect of Kaolin on Melting Characteristics of GGW

The aluminium content of GGW ash was boosted on mixing with kaolin. A substantially higher Al/Si ratio in the combustion residues of S10 compared with S9 explained why the former did not show any signs of melting, whereas the ash of the GGW sample containing 4 wt% of kaolin (S9) kept a hard sintered structure indicating that the ash passed through the melting stage (Fig. 16). This is because the higher the Al content in a fuel, the higher its capacity to form high-melting K-Al-silicates instead of K-silicates due to the greater affinity of K-species to react with Al in Si-rich systems increasing the ash melting points of coal and biomass fuels [9, 10, 44].

Identification of high melting crystalline K-species with increased K contents in the ash of kaolin-doped GGW samples (S9, S10) confirmed that kaolin helped bind K into the ash as reported by other studies [7], whereas negligible S contents in both S9 and S10 combustion residues certified the poor S retention capability of kaolin [8–11].

Crystalline Compounds in Kaolin doped GGW XRD analysis of the ash residues of S9 (GGW—4 wt% kaolin mixture) revealed the presence of different high melting potassium aluminium silicates (($KAlSiO_4$), sanidine ($K_{0.41}Na_{0.56}Ca_{0.03}$ $(Al_{1.03}Si_{2.97})O_8$), jadeite ($NaAlSi_2O_6$) and leucite ($KAlSi_2O_6$)) which were absent in the ash residues of crude GGW (S1) (Table 5). These relatively higher melting potassium-aluminium silicates have also been reported in the ashes of non-woody biomass fuels whose ash melting

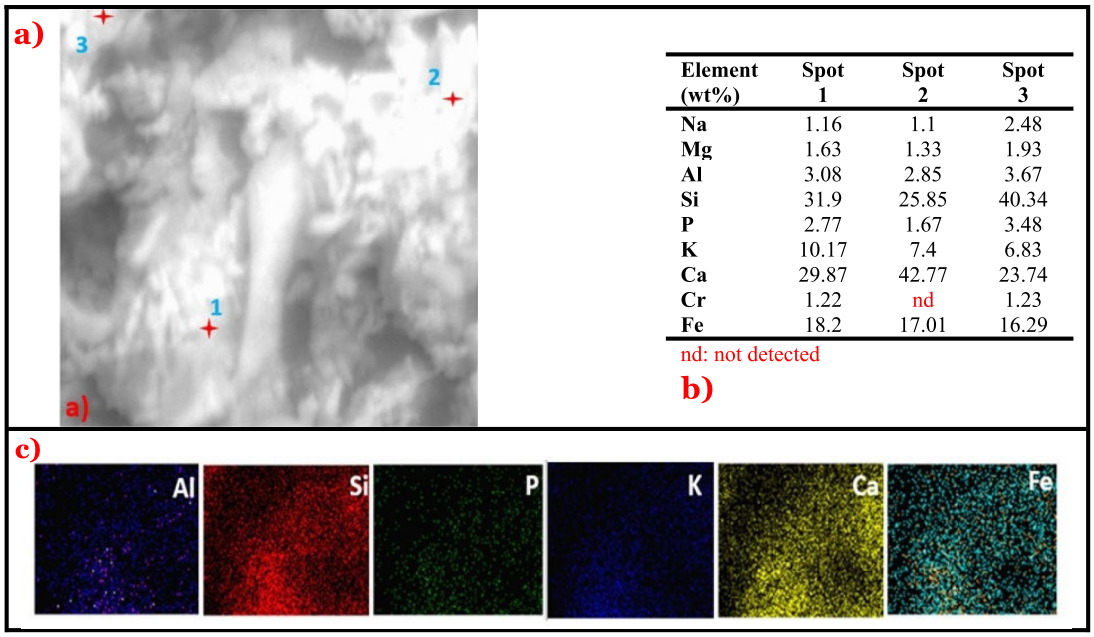

Element (wt%)	Spot 1	Spot 2	Spot 3
Na	1.16	1.1	2.48
Mg	1.63	1.33	1.93
Al	3.08	2.85	3.67
Si	31.9	25.85	40.34
P	2.77	1.67	3.48
K	10.17	7.4	6.83
Ca	29.87	42.77	23.74
Cr	1.22	nd	1.23
Fe	18.2	17.01	16.29

nd: not detected

Fig. 8 **a** SEM micrograph of combusted residues of S2 (GGW—4 wt% CaO mixture) at the magnification of 5000×, **b** average composition of the EDX scanned points, **c** concentrational profile of the elemental maps

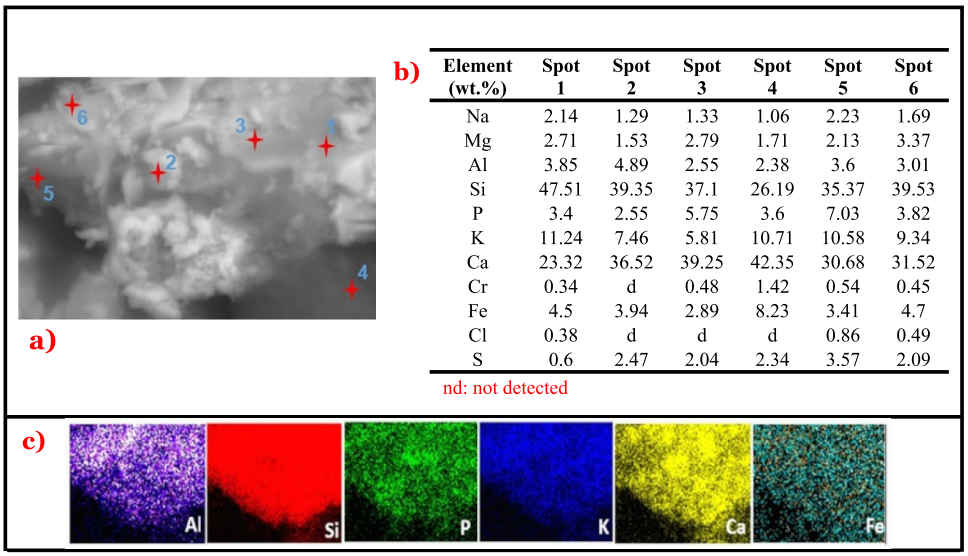

Element (wt.%)	Spot 1	Spot 2	Spot 3	Spot 4	Spot 5	Spot 6
Na	2.14	1.29	1.33	1.06	2.23	1.69
Mg	2.71	1.53	2.79	1.71	2.13	3.37
Al	3.85	4.89	2.55	2.38	3.6	3.01
Si	47.51	39.35	37.1	26.19	35.37	39.53
P	3.4	2.55	5.75	3.6	7.03	3.82
K	11.24	7.46	5.81	10.71	10.58	9.34
Ca	23.32	36.52	39.25	42.35	30.68	31.52
Cr	0.34	d	0.48	1.42	0.54	0.45
Fe	4.5	3.94	2.89	8.23	3.41	4.7
Cl	0.38	d	d	d	0.86	0.49
S	0.6	2.47	2.04	2.34	3.57	2.09

nd: not detected

Fig. 9 **a** SEM micrograph of combusted residues of S3 (GGW—4 wt% CES mixture) at the magnification of 5000×, **b** average composition of the EDX scanned points, **c** concentrational profile of the elemental maps

was mitigated entirely through kaolin by restraining the formation of K-silicates [8–10, 23, 38, 44].

This implies that kaolin reacted with K-species (such as KCl,K_2CO_3,K_2SO_4,KOH), leading to the formation of high potassium aluminium silicates (through reactions R8–R15) [13].

$$2KOH + Al_2Si_2O_5(OH)_4 \rightarrow 2KAlSiO_4 + 3H_2O \quad (R8)$$

$$2KCl + Al_2Si_2O_5(OH)_4 \rightarrow 2KAlSiO_4 + 2HCl + H_2O \quad (R9)$$

$$K_2SO_4 + Al_2Si_2O_5(OH)_4 \rightarrow 2KAlSiO_4 + SO_3 + 2H_2O \quad (R10)$$

$$K_2CO_3 + Al_2Si_2O_5(OH)_4 \rightarrow 2KAlSiO_4 + CO_2 + 2H_2O \quad (R11)$$

$$2KOH + Al_2Si_2O_5(OH)_4 + 2SiO_2 \rightarrow 2KAlSi_2O_6 + 3H_2O \quad (R12)$$

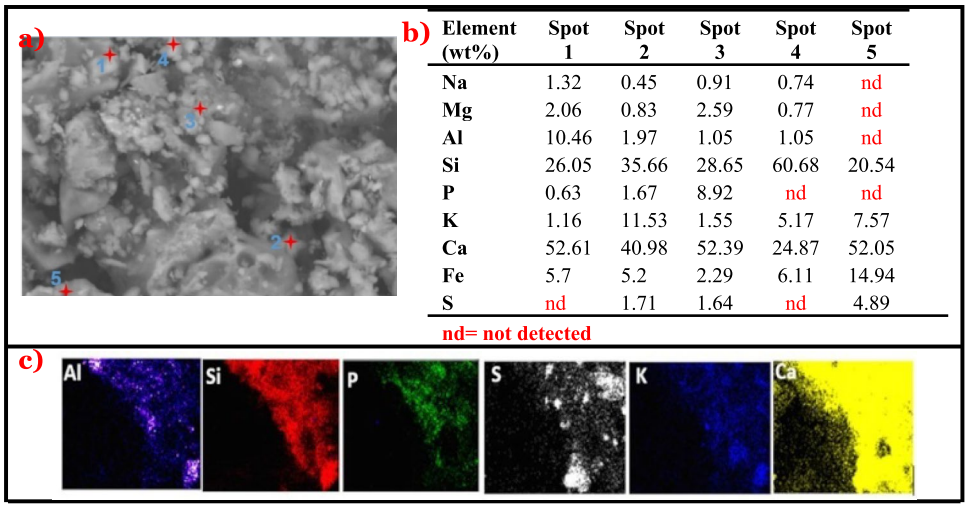

Element (wt%)	Spot 1	Spot 2	Spot 3	Spot 4	Spot 5
Na	1.32	0.45	0.91	0.74	nd
Mg	2.06	0.83	2.59	0.77	nd
Al	10.46	1.97	1.05	1.05	nd
Si	26.05	35.66	28.65	60.68	20.54
P	0.63	1.67	8.92	nd	nd
K	1.16	11.53	1.55	5.17	7.57
Ca	52.61	40.98	52.39	24.87	52.05
Fe	5.7	5.2	2.29	6.11	14.94
S	nd	1.71	1.64	nd	4.89

nd= not detected

Fig. 10 **a** SEM micrograph of combusted residues of S4 (GGW—8 wt% CES mixture) at the magnification of 5000×, **b** average composition of the EDX scanned points, **c** concentrational profile of the elemental maps

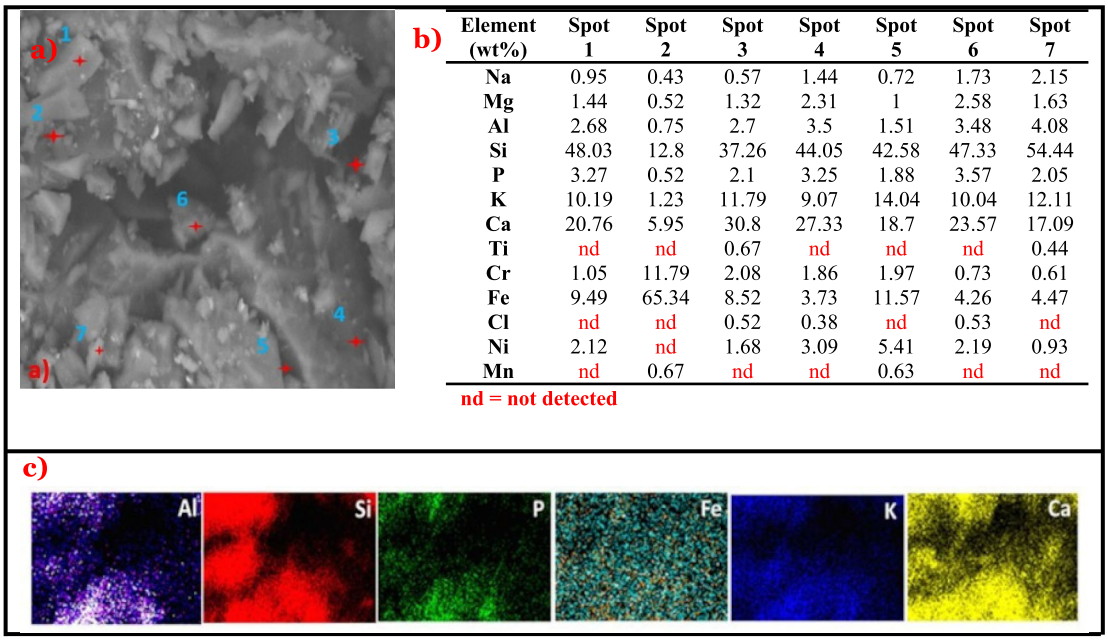

Element (wt%)	Spot 1	Spot 2	Spot 3	Spot 4	Spot 5	Spot 6	Spot 7
Na	0.95	0.43	0.57	1.44	0.72	1.73	2.15
Mg	1.44	0.52	1.32	2.31	1	2.58	1.63
Al	2.68	0.75	2.7	3.5	1.51	3.48	4.08
Si	48.03	12.8	37.26	44.05	42.58	47.33	54.44
P	3.27	0.52	2.1	3.25	1.88	3.57	2.05
K	10.19	1.23	11.79	9.07	14.04	10.04	12.11
Ca	20.76	5.95	30.8	27.33	18.7	23.57	17.09
Ti	nd	nd	0.67	nd	nd	nd	0.44
Cr	1.05	11.79	2.08	1.86	1.97	0.73	0.61
Fe	9.49	65.34	8.52	3.73	11.57	4.26	4.47
Cl	nd	nd	0.52	0.38	nd	0.53	nd
Ni	2.12	nd	1.68	3.09	5.41	2.19	0.93
Mn	nd	0.67	nd	nd	0.63	nd	nd

nd = not detected

Fig. 11 **a** SEM micrograph of combusted residues of S5 (GGW—4 wt% LS mixture) at the magnification of 5000×, **b** average composition of the EDX scanned points, **c** concentrational profile of the elemental maps

$$2KCl + Al_2Si_2O_5(OH)_4 + 2SiO_2 \rightarrow 2KAlSi_2O_6 + 2HCl + H_2O \quad \text{(R13)}$$

$$K_2SO_4 + Al_2Si_2O_5(OH)_4 + 2SiO_2 \rightarrow 2KAlSi_2O_6 + SO_3 + 2H_2O \quad \text{(R14)}$$

$$K_2Si_2O_{5(l)} + Al_2Si_2O_5(OH)_{4(s)} + 2SiO_{2(s)} \rightarrow 2KAlSi_3O_{8(s)} + 2H_2O_{(g)} \quad \text{(R15)}$$

Since these K-Al-silicates have significantly higher melting points (i.e. over 1000 °C) as compared to K-silicates (who melt in the range of 700–1400 °C depending upon the Si-content in the fuel ash) they substantially increase the AFT of GGW and thus substantially reduce melting [38].

In addition to these high melting K-aluminosilicates, potassium calcium iron phosphate ($KCaFe(PO_4)_2$) and quartz (SiO_2) were also identified in the ash residues of

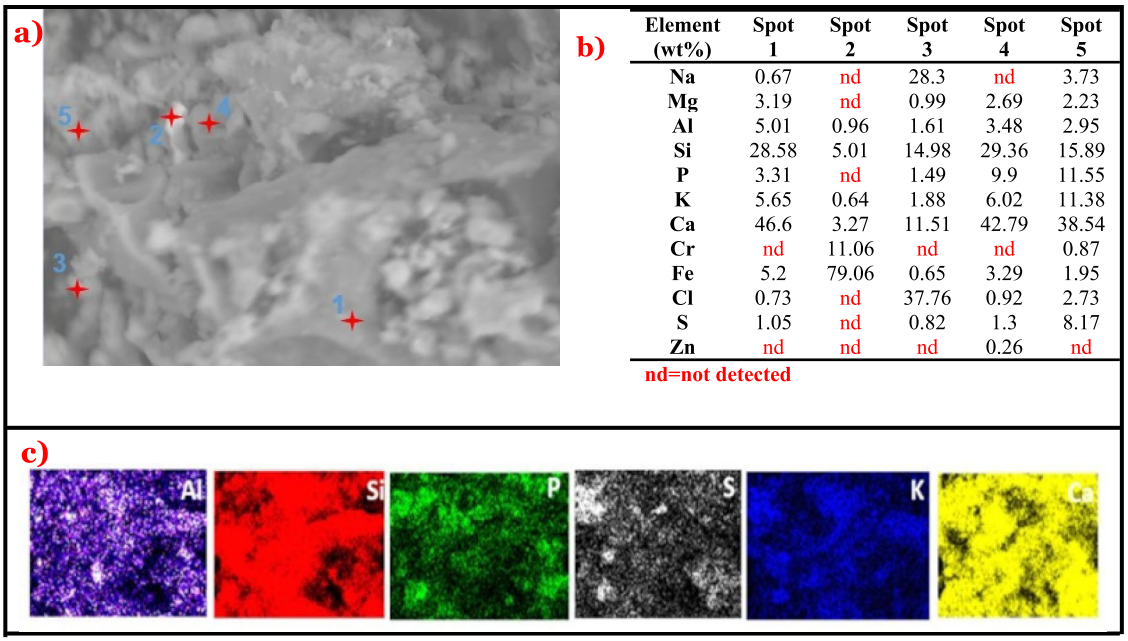

Element (wt%)	Spot 1	Spot 2	Spot 3	Spot 4	Spot 5
Na	0.67	nd	28.3	nd	3.73
Mg	3.19	nd	0.99	2.69	2.23
Al	5.01	0.96	1.61	3.48	2.95
Si	28.58	5.01	14.98	29.36	15.89
P	3.31	nd	1.49	9.9	11.55
K	5.65	0.64	1.88	6.02	11.38
Ca	46.6	3.27	11.51	42.79	38.54
Cr	nd	11.06	nd	nd	0.87
Fe	5.2	79.06	0.65	3.29	1.95
Cl	0.73	nd	37.76	0.92	2.73
S	1.05	nd	0.82	1.3	8.17
Zn	nd	nd	nd	0.26	nd

nd=not detected

Fig. 12 **a** SEM micrograph of combusted residues of S6 (GGW—8 wt% LS mixture) at the magnification of 5000×, **b** average composition of the EDX scanned points, **c** concentrational profile of the elemental maps

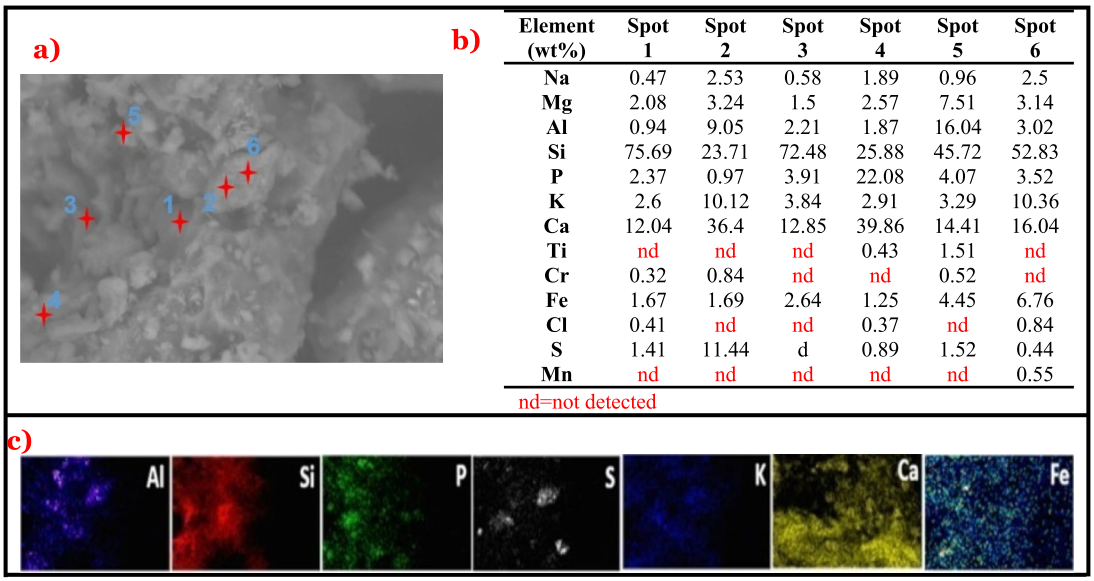

Element (wt%)	Spot 1	Spot 2	Spot 3	Spot 4	Spot 5	Spot 6
Na	0.47	2.53	0.58	1.89	0.96	2.5
Mg	2.08	3.24	1.5	2.57	7.51	3.14
Al	0.94	9.05	2.21	1.87	16.04	3.02
Si	75.69	23.71	72.48	25.88	45.72	52.83
P	2.37	0.97	3.91	22.08	4.07	3.52
K	2.6	10.12	3.84	2.91	3.29	10.36
Ca	12.04	36.4	12.85	39.86	14.41	16.04
Ti	nd	nd	nd	0.43	1.51	nd
Cr	0.32	0.84	nd	nd	0.52	nd
Fe	1.67	1.69	2.64	1.25	4.45	6.76
Cl	0.41	nd	nd	0.37	nd	0.84
S	1.41	11.44	d	0.89	1.52	0.44
Mn	nd	nd	nd	nd	nd	0.55

nd=not detected

Fig. 13 **a** SEM micrograph of combusted residues of S7 (GGW—4 wt% RES mixture) at the magnification of 5000×, **b** average composition of the EDX scanned points, **c** concentrational profile of the elemental maps

S9, which also seemingly contributed to the enhancement of the ash melting characteristics of GGW ash [45]. Diopside ($Ca_{0.964}Mg(Si_2O_6)$ which is a low melting crystalline phase was identified in S9 ashes by XRD analysis, but it was not identified in the ash residues of non-melted S10 GGW—8 wt% kaolin mixture). This was because the amount of the kaolin added in S9 was insufficient to completely restrain the formation of low-melting K-silicates and the compounds that tend to make eutectics with them. On the other hand, XRD diffractogram of ash residues containing 8 wt% of kaolin (S10) exhibited higher contents of K-Al-silicates (such as leucite ($KAlSi_2O_6$), $K(AlSi_3O_8)$, and

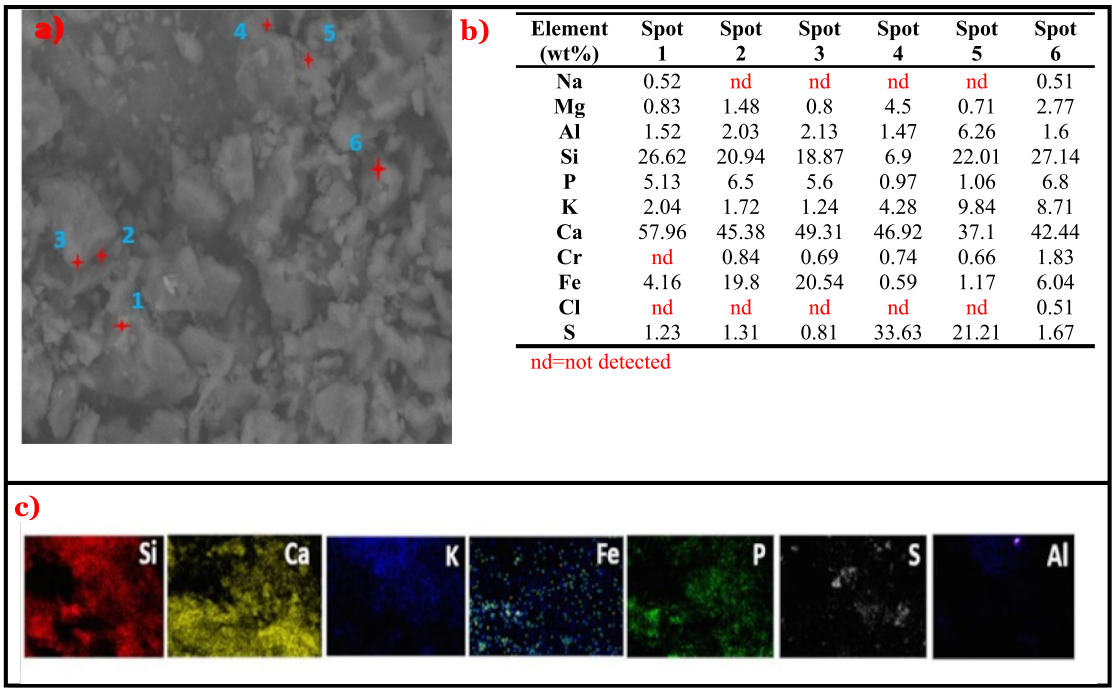

Element (wt%)	Spot 1	Spot 2	Spot 3	Spot 4	Spot 5	Spot 6
Na	0.52	nd	nd	nd	nd	0.51
Mg	0.83	1.48	0.8	4.5	0.71	2.77
Al	1.52	2.03	2.13	1.47	6.26	1.6
Si	26.62	20.94	18.87	6.9	22.01	27.14
P	5.13	6.5	5.6	0.97	1.06	6.8
K	2.04	1.72	1.24	4.28	9.84	8.71
Ca	57.96	45.38	49.31	46.92	37.1	42.44
Cr	nd	0.84	0.69	0.74	0.66	1.83
Fe	4.16	19.8	20.54	0.59	1.17	6.04
Cl	nd	nd	nd	nd	nd	0.51
S	1.23	1.31	0.81	33.63	21.21	1.67

nd=not detected

Fig. 14 **a** SEM micrograph of combusted residues of S8 (GGW—8 wt% RES mixture) at the magnification of 5000×, **b** average composition of the EDX scanned points, **c** concentration profile of the elemental maps

$K_{0.95}(AlSi_3O_8)$ as compared to S9 signalling to the complete consumption of K-species by aluminosilicates introduced through kaolin. High melting anorthite, sodian [46, 47] and hematite [48], were also identified in S10 while they were absent in S9. Formation of anorthite, sodian implies the reaction between aluminosilicates introduced by kaolin and Ca [8, 45]. Furthermore, excess Si and P ended up as quartz and potassium calcium iron phosphate ($KCaFe(PO_4)_2$) in both S9 and S10, and they contributed to enhancing the AFT of GGW due to their significantly higher melting points and refractory nature [45]. The characteristic ash melting features of kaolin-dopped GGW samples are shown in Fig. 17.

Surface Features of Ash Residues of Kaolin Doped GGW Samples The appearance of smooth homogenous regions in the SEM-micrograph of the ash residues of S9 (Fig. 16) evidently confirms that they were partially melted, whereas the surface of ash residues of S10 (Fig. 18) looked more compact with particles of different sizes with minimal or no continuous areas indicating the lack of melted particles. Furthermore, in SEM-micrographs of both S9 and S10 ash samples, K, Si, and Al were the three main elements detected from the most scanned EDX spots (Figs. 16, 18) and clear overlapping can be observed between their elemental maps with that of Ca and P, which plausibly indicates the co-presence of potassium calcium iron phosphate ($KCaFe(PO_4)_2$) with K-aluminosilicates which was in agreement with identification of these phases in XRD analysis (Table 5). EDX spot 1 in Fig. 16a (which represents combustion residues of S9) with Si + K contents = 84.43% possibly indicates the presence of melted K-silicates in the partially fused ash residues of S9, which contain 4 wt% of kaolin. It is likely that they were present in amorphous form and thus were not revealed by XRD, or their amount was too small to generate strong response signals in the XRD diffractogram.

Effect of ADP on Combustion Characteristics of GGW

As expected, both elemental and crystalline phase analysis of S11 and S12 ashes by XRD (Table 5) confirmed that the addition of P through ADP considerably increased the P/K and P/Ca ratios in the GGW, facilitating the formation of high melting ternary/quaternary phosphates of potassium and calcium (such as $Ca_{2.71}Mg_{0.29}(PO_4)_2$, $KCaFe(PO_4)_2$,$CaFe_5(PO_4)_5(OH)(H_2O)$, $Ca_9MgK(PO_4)_7$) instead of low melting K-silicates or pure phosphates of K and Ca which contributed to increasing the AFT.

The increase in the AFT of S11 can be attributed to the detection of high melting phases like $KCaFe(PO_4)_2$ and Ca-silicate (pseudowollastonite) in its combustion residues, which were not present in the S1 residues. $KCaFe(PO_4)_2$ in the combustion residues of S11 confirmed the K binding properties of ADP into ash, as reported in other similar studies [19]. However, identification of the phases such as Ca-Mg-silicate and whitlockite (which were also observed in the melted ashes of crude GGW (S1) in the partially sintered

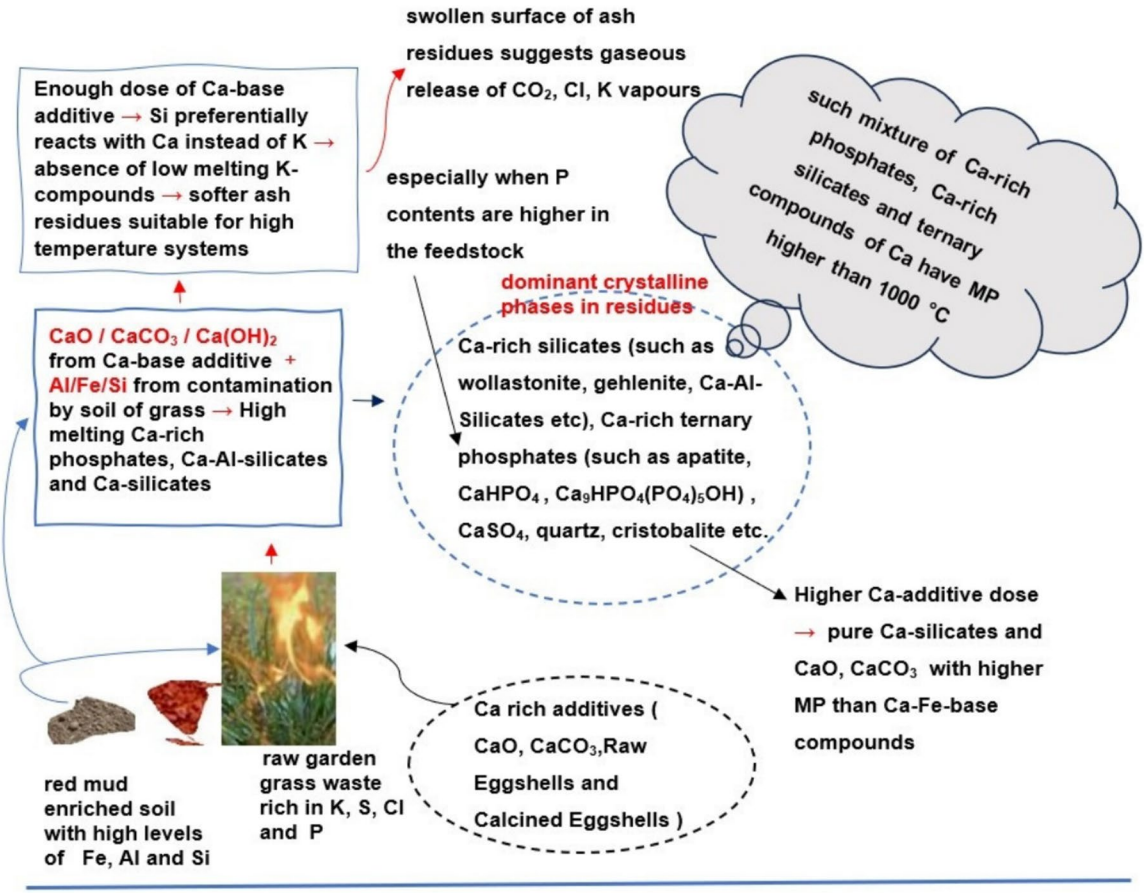

Fig. 15 Important features of melting characteristics of ash of Ca-dopped mixtures of garden grass waste (GGW)

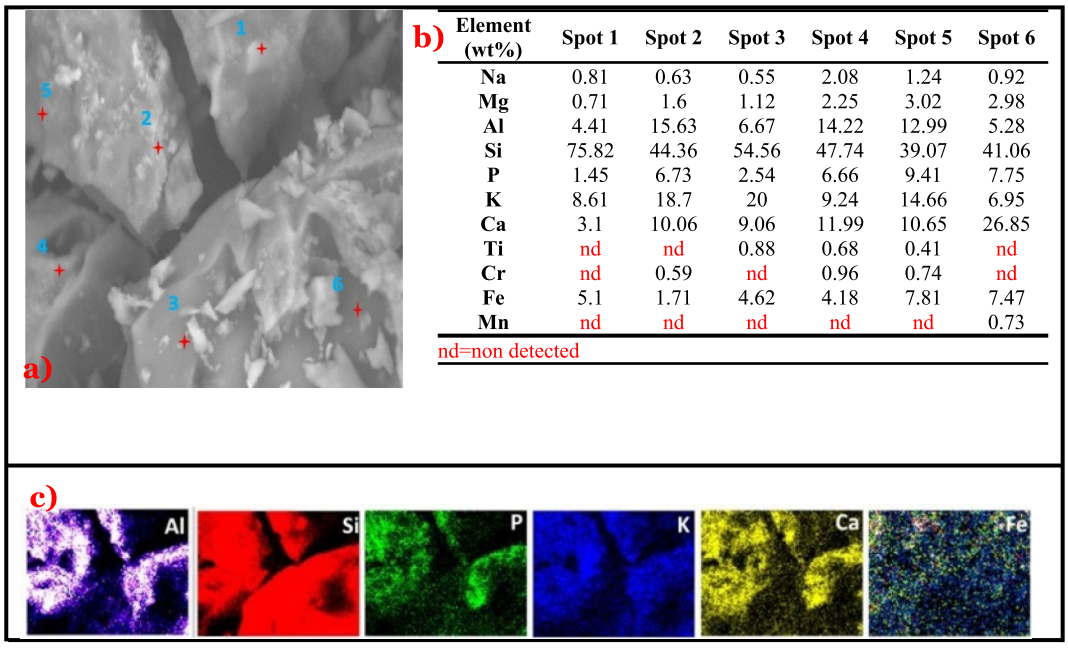

Element (wt%)	Spot 1	Spot 2	Spot 3	Spot 4	Spot 5	Spot 6
Na	0.81	0.63	0.55	2.08	1.24	0.92
Mg	0.71	1.6	1.12	2.25	3.02	2.98
Al	4.41	15.63	6.67	14.22	12.99	5.28
Si	75.82	44.36	54.56	47.74	39.07	41.06
P	1.45	6.73	2.54	6.66	9.41	7.75
K	8.61	18.7	20	9.24	14.66	6.95
Ca	3.1	10.06	9.06	11.99	10.65	26.85
Ti	nd	nd	0.88	0.68	0.41	nd
Cr	nd	0.59	nd	0.96	0.74	nd
Fe	5.1	1.71	4.62	4.18	7.81	7.47
Mn	nd	nd	nd	nd	nd	0.73

nd=non detected

Fig. 16 **a** SEM micrograph of combusted residues of S9 (GGW—4 wt% kaolin mixture) at the magnification of 5000×, **b** average composition of the EDX scanned points, **c** concentrational profile of the elemental maps

ash residues of S11 (GGW + 4 wt% ADP) indicated that the amount of P added in S11 wasn't sufficient to completely inhibit the formation of low-melting phases which made the combustion residues hard as stone.

Furthermore, the partial replacement of Si available to react with K by P increased the amount of free unreacted silica in the ash (appeared as cristobalite and quartz by XRD in Table 5), which also seemingly contributed to enhancing the melting characteristics of GGW ash. Though no evident K-silicates\phosphates were identified in the XRD diffractogram of S11, the presence of low-melting K-silicates/ phosphates in the amorphous form in its ash melt is very likely.

Contrary to S11, only high melting compounds were identified in the ash residues of S12 (mixture of GGW and 8 wt% ADP) that didn't melt at all (Table 5). Especially, considerably higher contents of high melting phosphates were detected, including aluminium phosphate ($Al(PO_4)$), potassium calcium magnesium phosphate ($Ca_9MgK(PO_4)_7$), potassium calcium iron phosphate ($KCaFe(PO_4)_2$), and calcium iron phosphate hydroxide hydrate ($CaFe_5(PO_4)_5(OH)(H_2O)$). So, XRD analysis of S12 confirmed the complete inhibition of the interaction between K-species with Si that form low-melting eutectic mixtures. The formation of K-Ca-phosphates and Ca-Fe-phosphates in the S12 ashes was in agreement with the previous studies that reported their presence in Ca, P and Fe-rich biomass ashes [19, 49] (Fig. 21 shows the chemistry of the samples doped with ADP). Alumino-minerals present in the ash of crude GGW

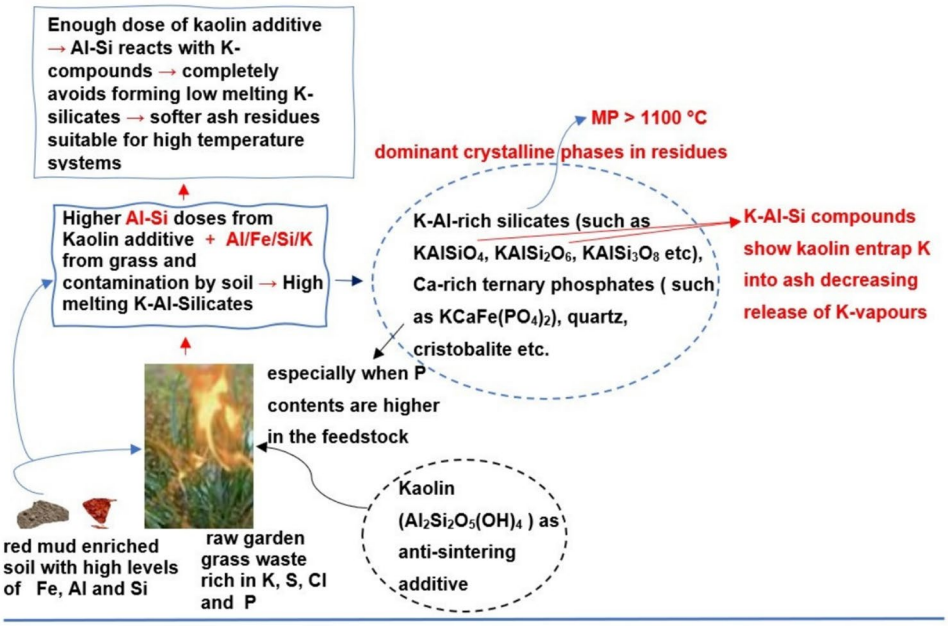

Fig. 17 Important features of melting characteristics of ash of kaolin-dopped mixtures of garden grass waste (GGW)

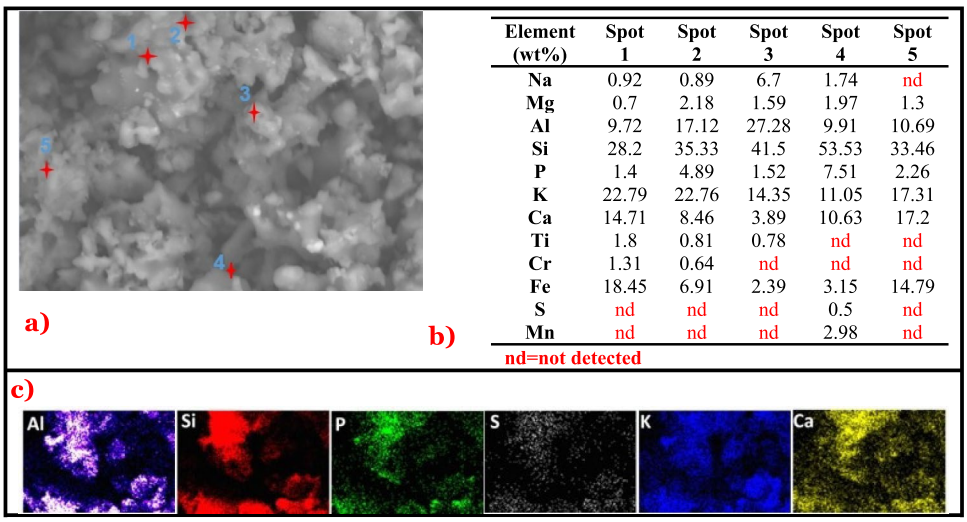

Element (wt%)	Spot 1	Spot 2	Spot 3	Spot 4	Spot 5
Na	0.92	0.89	6.7	1.74	nd
Mg	0.7	2.18	1.59	1.97	1.3
Al	9.72	17.12	27.28	9.91	10.69
Si	28.2	35.33	41.5	53.53	33.46
P	1.4	4.89	1.52	7.51	2.26
K	22.79	22.76	14.35	11.05	17.31
Ca	14.71	8.46	3.89	10.63	17.2
Ti	1.8	0.81	0.78	nd	nd
Cr	1.31	0.64	nd	nd	nd
Fe	18.45	6.91	2.39	3.15	14.79
S	nd	nd	nd	0.5	nd
Mn	nd	nd	nd	2.98	nd

nd=not detected

Fig. 18 **a** SEM micrograph of combusted residues of S10 (GGW—8 wt% kaolin mixture) at the magnification of 5000×, **b** average composition of the EDX scanned points, **c** concentrational profile of the elemental maps

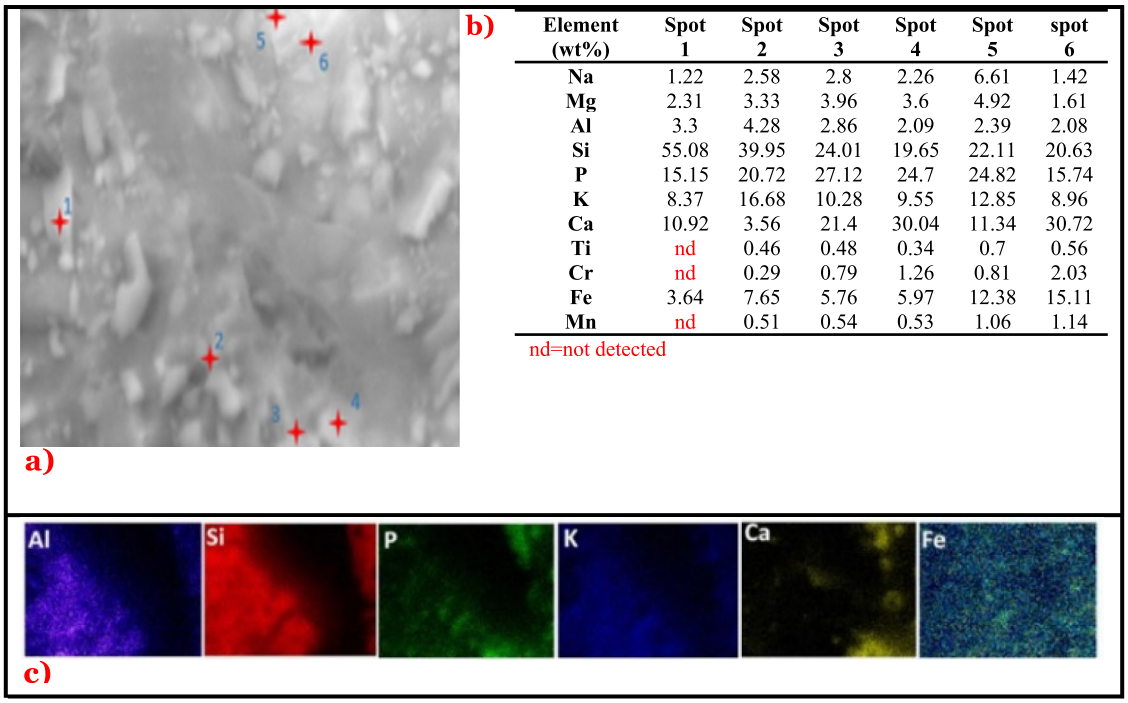

Element (wt%)	Spot 1	Spot 2	Spot 3	Spot 4	Spot 5	spot 6
Na	1.22	2.58	2.8	2.26	6.61	1.42
Mg	2.31	3.33	3.96	3.6	4.92	1.61
Al	3.3	4.28	2.86	2.09	2.39	2.08
Si	55.08	39.95	24.01	19.65	22.11	20.63
P	15.15	20.72	27.12	24.7	24.82	15.74
K	8.37	16.68	10.28	9.55	12.85	8.96
Ca	10.92	3.56	21.4	30.04	11.34	30.72
Ti	nd	0.46	0.48	0.34	0.7	0.56
Cr	nd	0.29	0.79	1.26	0.81	2.03
Fe	3.64	7.65	5.76	5.97	12.38	15.11
Mn	nd	0.51	0.54	0.53	1.06	1.14

nd=not detected

Fig. 19 **a** SEM micrograph of combusted residues of S11 (GGW—4 wt% ADP mixture) at the magnification of 5000×, **b** average composition of the EDX scanned points, **c** concentrational profile of the elemental maps

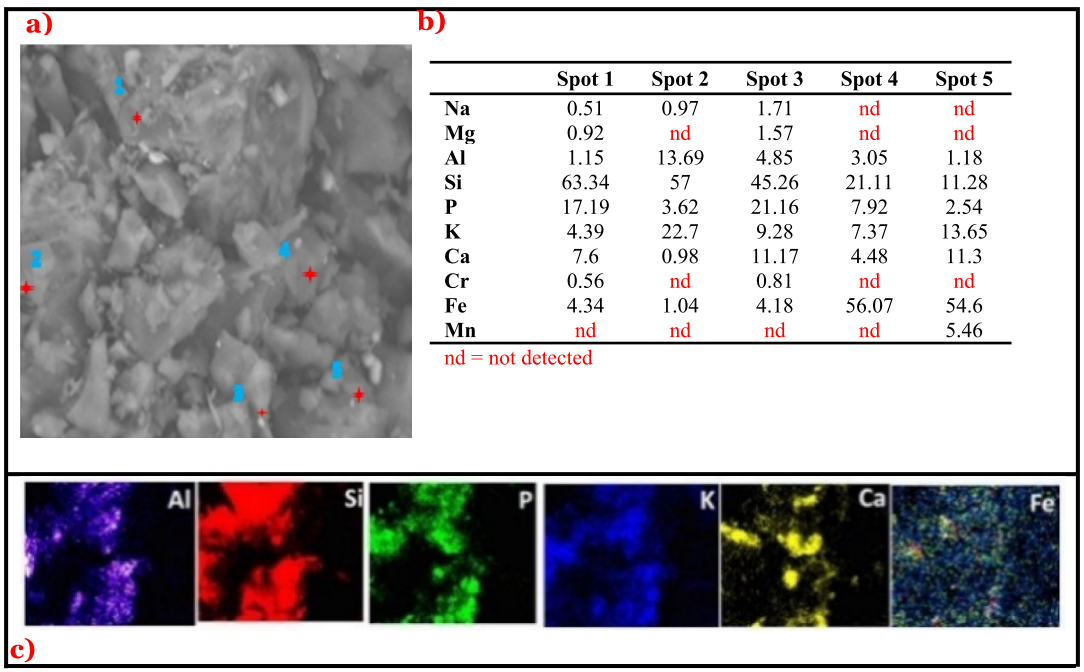

	Spot 1	Spot 2	Spot 3	Spot 4	Spot 5
Na	0.51	0.97	1.71	nd	nd
Mg	0.92	nd	1.57	nd	nd
Al	1.15	13.69	4.85	3.05	1.18
Si	63.34	57	45.26	21.11	11.28
P	17.19	3.62	21.16	7.92	2.54
K	4.39	22.7	9.28	7.37	13.65
Ca	7.6	0.98	11.17	4.48	11.3
Cr	0.56	nd	0.81	nd	nd
Fe	4.34	1.04	4.18	56.07	54.6
Mn	nd	nd	nd	nd	5.46

nd = not detected

Fig. 20 **a** SEM micrograph of combusted residues of S12 (GGW—8 wt% ADP mixture) at the magnification of 5000×, **b** average composition of the EDX scanned points, **c** concentrational profile of the elemental maps

(that possibly came through soil contamination) seems to have reacted with P at high temperature forming $AlPO_4$ (MP 2000 °C) in combustion residues of GGW—8 wt% ADP mixture [50] which seemingly acted as a refractory phase and improved the ash fusion characteristics of the S12 ADP doped GGW sample. Notably, the absence of S from the elemental composition and diffractograms of ash residues of the ADP doped GGW samples (S11, S12) indicated that the enhancement of P contents of GGW reduced the chance for S to react with gaseous K or Ca, suggesting in the extensive release of SO_2 [51].

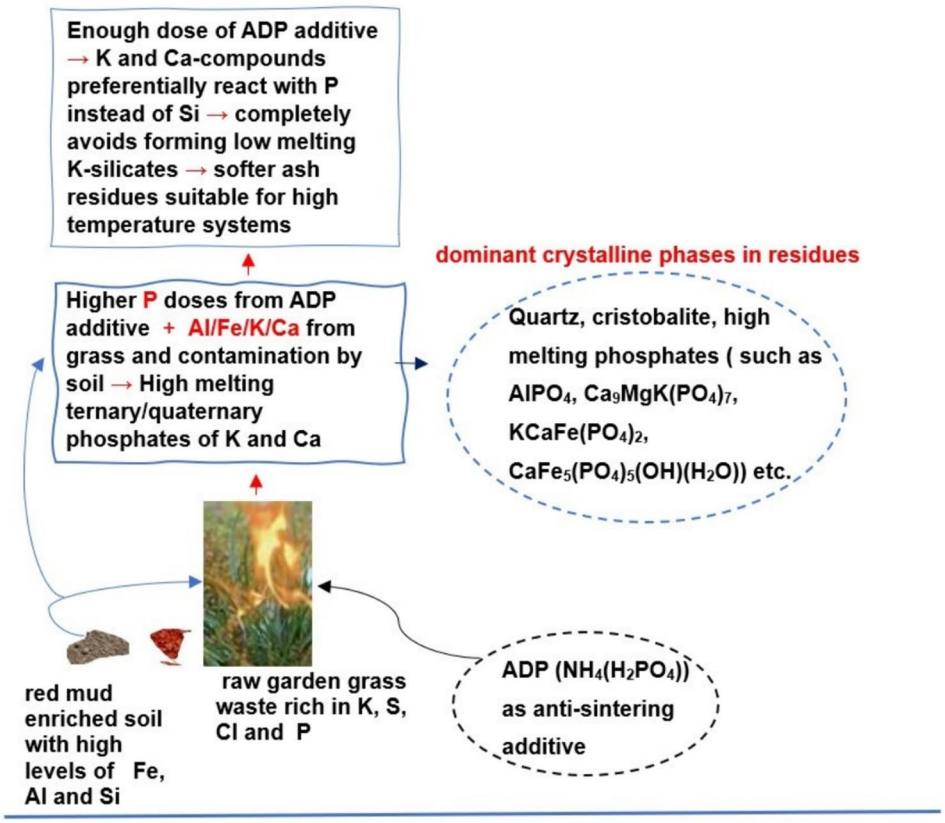

Fig. 21 Important features of melting characteristics of ash of ADP-dopped mixtures of garden grass waste (GGW)

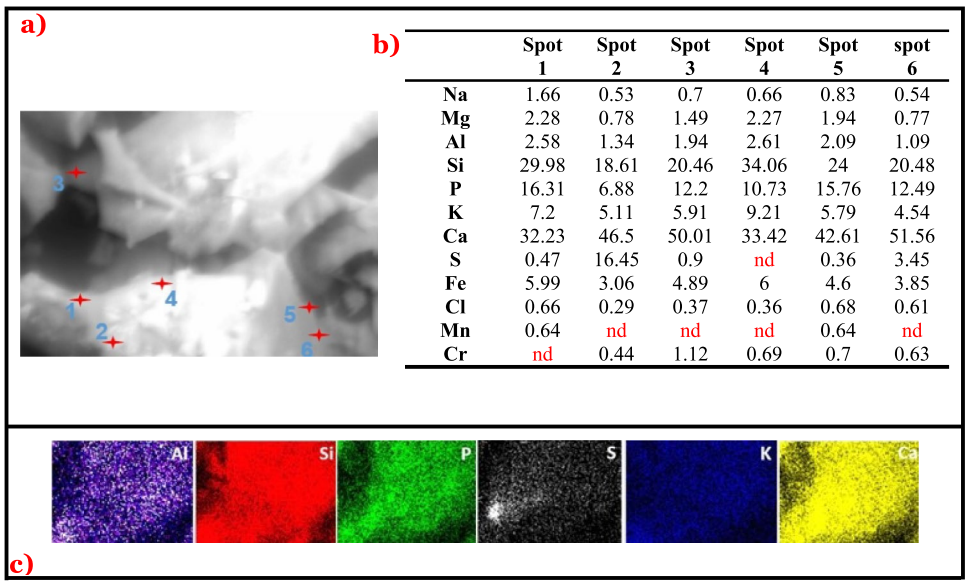

	Spot 1	Spot 2	Spot 3	Spot 4	Spot 5	spot 6
Na	1.66	0.53	0.7	0.66	0.83	0.54
Mg	2.28	0.78	1.49	2.27	1.94	0.77
Al	2.58	1.34	1.94	2.61	2.09	1.09
Si	29.98	18.61	20.46	34.06	24	20.48
P	16.31	6.88	12.2	10.73	15.76	12.49
K	7.2	5.11	5.91	9.21	5.79	4.54
Ca	32.23	46.5	50.01	33.42	42.61	51.56
S	0.47	16.45	0.9	nd	0.36	3.45
Fe	5.99	3.06	4.89	6	4.6	3.85
Cl	0.66	0.29	0.37	0.36	0.68	0.61
Mn	0.64	nd	nd	nd	0.64	nd
Cr	nd	0.44	1.12	0.69	0.7	0.63

Fig. 22 **a** SEM micrograph of combusted residues of S13 (GGW—4 wt% CES—4 wt% ADP mixture) at the magnification of 5000×, **b** average composition of the EDX scanned points, **c** concentrational profile of the elemental maps

Effect of ADP on Morphology of Ash Residues of GGW SEM-micrographs of the ash residues of ADP and GGW mixtures (S11, S12) appeared significantly different from the residues of crude GGW (S1 in Fig. 4a).The surface of the partially melted residues of S11 showed plain continuous regions with some irregularly-shaped embedded crystalline particles (Fig. 19a) confirming the presence of melted amorphous phases in non-melted ash particles that resulted in hard sintered residues. However, the surface of ash particles of S12 (in Fig. 20a), which were not melted at all, didn't show any smooth region and predominantly illustrated abruptly placed particles of different sizes.

Considerably higher contents of Si, P and K and lower amounts of Ca at EDX spot 2 in the SEM-micrograph of the ashes of S11 (Fig. 19a) eluded to the existence of amorphous melted phases (possibly pure K-silicates and K-phosphates) that were not observed in the XRD results which supported the requirement of more P to completely subdue the formation of the low-melting compounds that hardened the combustion residues of S11 as confirmed by visual sintering evaluation results ("Visual Evaluation of Sintering Tendency of Crude and Additive Modulated Mixtures of GGW" section) and XRD (Table 5).

Evaluation of Combined Anti-Sintering Characteristics of ADP & CES Mixed Additives` Stream

GGW samples mixed with both P and Ca-rich additives in the form of ADP and CES, each in 4 wt% proportion, helped in complete inhibition of ash melting, but the performance was not better than the respective pure streams when used in 8 wt% proportion (i.e., of 8 wt% CES based S4 and 8 wt% ADP doped S12). Nor were any synergistic effects observed from using a mixed additive stream. This more likely happened because the co-existence of Ca-rich silicate and phosphates may have generated minute amounts of low-melting eutectic systems in the amorphous form [52]. The XRD diffractogram showed that addition of both additives in parallel favoured the formation of high melting Ca-rich silicates (such as pseudowollastonite, $Ca_3(Si_3O_9)$; wollastonite, $Ca_{0.957}Fe_{0.043}O_3Si$, potassium calcium silicate, $K_4CaSi_3O_9$) and binded K into the ash as high melting Ca-rich phosphates (such as $Ca_9MgK(PO_4)_7$, $KCaFe(PO_4)_2$). The formation of these compounds with high melting refractory phases, such as quartz, cristobalite, hydroxylapatite and calcium hydrogen phosphate hydrate (Table 5), also contributed to enhancing the melting characteristics of GGW ash. From this, we can plausibly assume that the ash system containing only Ca-rich phosphates or Ca-rich silicates would have a higher AFT than the one containing a mixture of both (Fig. 21).

Effect of Mixed Additive Streams on Microchemistry and Morphology of GGW Ash The SEM micrograph of S13 (Fig. 22a) also supported the positive influence of a mixed ADP and CES additive stream on the ash melting at a microcosmic morphology. Interaction between the elemental maps of the most dominant elements of S13 ash (such as Ca 31.63%, Si 31.55%, P 14.18%, and K 6.85% as per Fig. 22b) was clearly distinguishable, which supported the formation of Ca-silicates and Ca-rich phosphates as illustrated by XRD analysis results (Table 5). The localised concentration of S in the elemental map (Fig. 22c) possibly represented the presence of $CaSO_4$ as indicated by high S (16.45%) and Ca (46.5%) contents detected at spot 2 of the SEM-micrograph of S13 (Fig. 22b).

Summary and Conclusions

XRD and SEM-EDX analysis results revealed that the ash of crude grass waste melts severely at high temperatures due to the formation of low-melting eutectic mixtures of K-silicates and phosphates. Adding lime, calcined eggshells, raw eggshells, limestone, ammonium dihydrogen phosphate, and kaolin in 8 wt% proportion into GGW completely mitigated the ash melting by restraining the formation of low-melting compounds and consequentially making the ash residues softer. GGW-8 wt% kaolin mixture resulted in the softest ash residues among all the additives tested. The addition of all additives in 4 wt% eliminated the slagging of GGW ash, and the ash residues didn't stick to the bottom of the test crucibles, but the residues were as hard as a stone, rendering this additive proportion insufficient and unsatisfactory. Both raw eggshells waste and calcined eggshells waste exhibited promising anti-sintering characteristics. Hence, they can be used as low-cost alternatives to commercially available limestone and lime in the biomass industry. Adding ADP and kaolin enhanced K retention into GGW ash, while Ca-based additives helped bind S into ash. No synergistic effects were observed on mixing both Ca and P-rich additive streams (CES and ADP 4 wt% each) into GGW, and ash residues containing either pure Ca additives or P additives in 8 wt% proportion were softer than the combustion residues of samples doped with both Ca and P rich streams. The AFT of biomass ash systems containing either pure Ca-rich silicates or Ca-rich phosphates would be higher than those containing both. Co-existence of Ca-rich silicate and phosphates can even generate low melting eutectic systems; the use of pure additive streams rich in either Ca or P contents should be preferred for anti-sintering purposes.

Acknowledgements This work was funded by Biogen Systems Ltd UK, University of Chester and the European Union Regional Development Fund (ERDF) through the Eco-Innovation Cheshire and Warrington project. The authors would like to thank the funding bodies, especially Julian Uhlig of Entrade Energiesysteme AG and Julian

Ackerley of Biogen Systems Ltd for providing the research training for this project. The authors would also like to thank Andy McLauchlin of Royce Institute and Prof Graham C. Smith of the University of Chester for their advice on SEM-EDS and XRD analysis for this work.

Author Contributions All authors contributed to the study's conception and design. M. Latif: conceptualization, investigation, methodology, data collection, formal analysis, writing-original draft; J.G. Brammer: supervision, writing-review & editing, resources, funding. J. Morris: resources. All authors read and approved the final manuscript.

Funding Funding was provided by European Regional Development Fund (ERDF) (Grant No. EICW-4F-44).

Data Availability Data can be made available on request.

Declarations

Competing interests The authors declare that they have no known competing financial interests or personal relationships that could have appeared to influence the work reported in this paper.

Declaration of Generative AI and Assisted Technologies in the Writing Process During the preparation of this work the authors used Gimp 2.10.34 in order to increase the resolution of the images used in the text. After using this tool, the authors reviewed and edited the content as needed and take full responsibility for the content of the publication.

References

1. French, K.E.: Assessing the bioenergy potential of grassland biomass from conservation areas in England. Land Use Policy **82**, 700–708 (2019). https://doi.org/10.1016/j.landusepol.2018.12.001
2. Shi, Y., Yuanyuan, D., Guofu, Y., et al.: The use of green waste from tourist attractions for renewable energy production: the potential and policy implications. Energy Policy **62**, 410–418 (2013). https://doi.org/10.1016/j.Enpol.2013.07.126
3. Siddiqui, H., Thengane, S.K., Sharma, S., Mahajani, S.M.: Revamping downdraft gasifier to minimize clinker formation for high-ash garden waste as feedstock. Biores. Technol. **266**, p220–p231 (2018). https://doi.org/10.1016/j.biortech.2018.06.086
4. Pradhan, P., Amit, A., Mahajani, M.S.: Pilot scale evaluation of fuel pellets production from garden waste biomass. Energy Sustain. Dev. **43**, p1–p14 (2018). https://doi.org/10.1016/j.Esd.2017.11.005
5. van der Weijde, T., Andreas, K., Yasir, I., et al.: Evaluation of *Miscanthus sinensis* biomass quality as feedstock for conversion into different bioenergy products. GCB Bioenergy. **9**(1), 176–190 (2017). https://doi.org/10.1111/gcbb.12355
6. Amaducci, S., Facciotto, G., Bergante, S., et al.: Biomass production and energy balance of herbaceous and woody crops on marginal soils in the Po Valley. GCB Bioenergy. (2016). https://doi.org/10.1111/gcbb.12341
7. Steenari, B.-M., Lundberg, A., Pettersson, H., Wilewska-Bien, M., Andersson, D.: Investigation of ash sintering during combustion of agricultural residues and the effect of additives. Energy Fuels **23**(11), p5655–p5662 (2009). https://doi.org/10.1021/ef900471u
8. Öhman, M., Boström, D., Nordin, A., Hedman, H.: Effect of kaolin and limestone addition on slag formation during combustion of wood fuels. Energy Fuels **18**(5), p1370–p1376 (2004). https://doi.org/10.1021/ef040025+
9. Niu, Y., Tan, H., Hui, S.: Ash-related issues during biomass combustion: Alkali-induced slagging, silicate melt-induced slagging (ash fusion), agglomeration, corrosion, ash utilization, and related countermeasures. Prog. Energy Combust. Sci. **52**, p1–p61 (2016). https://doi.org/10.1016/j.pecs.2015.09.003
10. Zhu, Y., Niu, Y., Tan, H., Wang, X.: Short review on the origin and countermeasure of biomass slagging in grate furnace. Front. Energy Res. (2014). https://doi.org/10.3389/fenrg.2014.00007
11. Miguez, J.L., Jacobo, P., Frank, B., et al.: Review of the use of additives to mitigate operational problems associated with the combustion of biomass with high content in ash-forming species. Renew. Sustain. Energy Rev. (2021). https://doi.org/10.1016/j.rser.2020.110502
12. Khalsa, J.H.A., Frank, D., Florian, B.: Foliage and grass as fuel pellets-small scale combustion of washed and mechanically leached biomass. Energies (2016). https://doi.org/10.3390/en9050361
13. Mack, R., Kuptz, D., Schön, C., Hartmann, H.: Combustion behavior and slagging tendencies of kaolin additivated agricultural pellets and of wood-straw pellet blends in a small-scale boiler. Biomass Bioenerg. **125**, p50–p62 (2019). https://doi.org/10.1016/j.biombioe.2019.04.003
14. Laca, A., Adriana, L., Mario, D.: Eggshell waste as catalyst: a review. J. Environ. Manage. **197**, 351–359 (2017). https://doi.org/10.1016/j.jenvman.2017.03.088
15. Ferraz, E., Gamelas, J.A.F., Coroado, J., Monteiro, C., Rocha, F.: Eggshell waste to produce building lime: calcium oxide reactivity, industrial, environmental and economic implications. Mater. Struct. **51**(5), 115 (2018). https://doi.org/10.1617/s11527-018-1243-7
16. Wang, L., Geir, S., John, E., Yvind, S.: Investigation of biomass ash sintering characteristics and the effect of additives. Energy Fuels **28**(1), p208–p218 (2014). https://doi.org/10.1021/ef401521c
17. Qi, J., Han, K., Wang, Q., Gao, J.: Carbonization of biomass: effect of additives on alkali metals residue, SO2 and NO emission of chars during combustion. Energy **130**, 560–569 (2017). https://doi.org/10.1016/j.energy.2017.04.109
18. Li, L., Ren, Q., Li, S., Lu, Q.: Effect of phosphorus on the behavior of potassium during the co-combustion of wheat straw with municipal sewage sludge. Energy Fuels **27**(10), p5923–p5930 (2013). https://doi.org/10.1021/ef401196y
19. Qi, J., Hui, L., Kuihua, H., et al.: Influence of ammonium dihydrogen phosphate on potassium retention and ash melting characteristics during combustion of biomass. Energy **102**, p244–p251 (2016). https://doi.org/10.1016/j.energy.2016.02.090
20. Zapata, S., Canalís, P., Royo, J., Gómez, M., Bartolomé, C.: Combustion performance of agropellets in an experimental fixed bed reactor versus a commercial grate boiler. Validation of ash behavior. ACS Omega **8**(32), 29485–29499 (2023). https://doi.org/10.1021/acsomega.3c03201
21. Hassan, K., Al-Abdeli, Y.M., Guzzomi, F., Yeoh, G.H.: An overview of processes and considerations in the modelling of fixed-bed

biomass combustion. Energy **88**, 946–972 (2015). https://doi.org/10.1016/j.Energy.2015.05.099
22. Vassilev, S.V., Vassileva, C.G., Petrova, N.L.: Thermal behaviour of biomass ashes in air and inert atmosphere with respect to their decarbonation. Fuel **314**, 122766 (2022). https://doi.org/10.1016/j.Fuel.2021.122766
23. Wang, L., Skreiberg, Ø., Becidan, M., Li, H.: Investigation of rye straw ash sintering characteristics and the effect of additives. Appl. Energy **162**, p1195–p1204 (2016). https://doi.org/10.1016/j.apenergy.2015.05.027
24. Ma, X., Fenghai, L., Mingjie, M., Yitian, F.: Investigation on blended ash fusibility characteristics of biomass and coal with high silica-alumina. Energy Fuels **31**(8), 7941–7951 (2017). https://doi.org/10.1021/acs.energyfuels.7b01070
25. Skrifvars, B.J., Moilanen, A., Lundqvist, R.: Characterization of biomass ashes. In: Proc. Applications of advanced technology to ash-related problems in boilers. Plenum Press. https://phyllis.nl/Biomass/View/1699. Accessed 7 Oct 2023
26. Bhavanam, A., Sastry, R.C.: Thermogravimetric analysis and characterisation of yard waste as a feedstock to gasification process. Presented at: ASME 2013 International Mechanical Engineering Congress and Exposition. https://doi.org/10.1115/IMECE2013-64415 (2013). Accessed 26 Aug 2022
27. Ligthart, F.: Bedagglomeratie en asafzetting tijdens wervelbed-vergassing en -verbranding van biomassa. Rapportage van een literatuurstudie naar de achtergronden. https://phyllis.nl/Biomass/View/987. Accessed 7 Oct 2023
28. Namkung, H., Joo, L.Y., Hyoung, P.J.C.J., et al.: Influence of herbaceous biomass ash pre-treated by alkali metal leaching on the agglomeration/sintering and corrosion behaviors. Energy **187**, 115950 (2019). https://doi.org/10.1016/j.energy.2019.115950
29. Vassilev, S.V., Baxter, D., Vassileva, C.G.: An overview of the behaviour of biomass during combustion: Part II. Ash fusion and ash formation mechanisms of biomass types. Fuel **117**, 152-p183 (2014). https://doi.org/10.1016/j.Fuel.2013.09.024
30. Yao, X., Zhao, Z., Li, J., Zhang, B., Zhou, H., Xu, K.: Experimental investigation of physicochemical and slagging characteristics of inorganic constituents in ash residues from gasification of different herbaceous biomass. Energy **198**, 117367 (2020). https://doi.org/10.1016/j.energy.2020.117367
31. Niu, Y., Du, W., Tan, H., et al.: Further study on biomass ash characteristics at elevated ashing temperatures: the evolution of K, Cl, S and the ash fusion characteristics. Bioresour. Technol. **129**, p642–p645 (2013). https://doi.org/10.1016/j.biortech.2012.12.065
32. Vassilev, S.V., Baxter, D., Andersen, L.K., Vassileva, C.G.: An overview of the composition and application of biomass ash. Part 1. Phase-mineral and chemical composition and classification. Fuel **105**, p40–p76 (2013). https://doi.org/10.1016/j.fuel.2012.09.041
33. Beidaghy Dizaji, H., Zeng, T., Hölzig, H., Bauer, J., Klöß, G., Enke, D.: Ash transformation mechanism during combustion of rice husk and rice straw. Fuel **307**, 121768 (2022). https://doi.org/10.1016/j.fuel.2021.121768
34. Hannl, T.K., Häggström, G., Hedayati, A., Skoglund, N., Kuba, M., Öhman, M.: Ash transformation during single-pellet gasification of sewage sludge and mixtures with agricultural residues with a focus on phosphorus. Fuel Process. Technol. **227**, 107102 (2022). https://doi.org/10.1016/j.fuproc.2021.107102
35. Näzelius, I.-L., Fagerström, J., Boman, C., Boström, D., Öhman, M.: Slagging in fixed-bed combustion of phosphorus-poor biomass: critical ash-forming processes and compositions. Energy Fuels **29**(2), 894–908 (2015). https://doi.org/10.1021/ef502531m
36. Kyonka, J.C., Cook, R.L.V.: The properties of feldspars and their use in whitewares. University of Illinois at Urbana Champaign, College of Engineering, Engineering Experiment Station, no 422. https://www.ideals.illinois.edu/items/4859 (1954)
37. Li, F., Yu, B., Zhao, W., et al.: Investigation on formation mechanisms of ash and deposit from cotton stalk vibrating grate boiler combustion based on their characteristics. Fuel **323**, 124446 (2022). https://doi.org/10.1016/j.fuel.2022.124446
38. Wang, L., Geir, S., Hustad, J.E., Morten, G., Øyvind, S.: Effects of additives on Barley Straw and husk ashes sintering characteristics. Energy Proc. **20**(1876), p30–p39 (2012). https://doi.org/10.1016/j.egypro.2012.03.005
39. Scala, F., Chirone, R.: An SEM/EDX study of bed agglomerates formed during fluidized bed combustion of three biomass fuels. Biomass Bioenerg. **32**(3), p252–p266 (2008). https://doi.org/10.1016/j.biombioe.2007.09.009
40. Häggström, G.: Experimental studies of ash transformation processes in thermochemical conversion of P-rich biomass and sludge. Licentiate thesis, comprehensive summary. Luleå tekniska universite. http://urn.kb.se/resolve?urn=urn:nbn:se:ltu:diva-78593 (2020). Accessed 21 Sept 2020
41. Davidsson, K.O., Steenari, B.M., Eskilsson, D.: Kaolin addition during biomass combustion in a 35 MW circulating fluidized-bed boiler. Energy Fuels **21**(4), p1959–p1966 (2007). https://doi.org/10.1021/ef070055n
42. Priyanto, D.E., Shunichiro, U., Naoki, S., Hidekazu, K., Tatsurou, T., Hitoshi, F.: Ash transformation by co-firing of coal with high ratios of woody biomass and effect on slagging propensity. Fuel **174**, p172–p179 (2016). https://doi.org/10.1016/j.fuel.2016.01.072
43. Llorente, M.J.F., Laplaza, J.M.M., Cuadrado, R.E., García, J.E.C.: Ash behaviour of lignocellulosic biomass in bubbling fluidised bed combustion. Fuel **85**(9), p1157–p1165 (2006). https://doi.org/10.1016/j.fuel.2005.11.019
44. Wang, L., Becidan, M., Skreiberg, Ø.: Sintering behavior of agricultural residues ashes and effects of additives. Energy Fuels **26**(9), p5917–p5929 (2012). https://doi.org/10.1021/ef3004366
45. Zhang, Q., Liu, H., Qian, Y., Xu, M., Li, W., Xu, J.: The influence of phosphorus on ash fusion temperature of sludge and coal. Fuel Process. Technol. **110**, p218–p226 (2013). https://doi.org/10.1016/j.fuproc.2012.12.018
46. Kong, L., Bai, J., Bai, Z., Guo, Z., Li, W.: Improvement of ash flow properties of low-rank coal for entrained flow gasifier. Fuel **120**, 122–129 (2014). https://doi.org/10.1016/j.fuel.2013.12.001
47. Zhang, L., Wang, J., Song, X., Bai, Y., Yao, M., Yu, G.: Influence of biomass ash additive on fusion characteristics of high-silicon-aluminum coal ash. Fuel **282**, 118876 (2020). https://doi.org/10.1016/j.fuel.2020.118876
48. Kirnbauer, F., Hofbauer, H.: The mechanism of bed material coating in dual fluidized bed biomass steam gasification plants and its impact on plant optimization. Powder Technol. **245**, p94–p104 (2013). https://doi.org/10.1016/j.powtec.2013.04.022
49. Wang, Q., Kuihua, H., Jie, G., Jiamin, W., Chunmei, L.: Investigation of Maize Straw Char Briquette ash fusion characteristics and the influence of phosphorus additives. Energy Fuels **31**(3), p2822–p2830 (2017). https://doi.org/10.1021/acs.energyfuels.7b00047
50. Li, F., Fan, H., Wang, X., Wang, T., Fang, Y.: Influences of phosphorus on ash fusion characteristics of coal and its regulation mechanism. Fuel **239**, p1338–p1350 (2019). https://doi.org/10.1016/j.fuel.2018.11.004
51. Grimm, A., Skoglund, N., Boström, D., Boman, C., Öhman, M.: Influence of phosphorus on alkali distribution during combustion of logging residues and wheat straw in a bench-scale fluidized bed. Energy Fuels **26**(5), p3012–p3023 (2012). https://doi.org/10.1021/ef300275e
52. Wang, Q., Han, K., Qi, J., Zhang, J., Li, H., Lu, C.: Investigation of potassium transformation characteristics and the influence of

additives during biochar briquette combustion. Fuel **222**, 407–415 (2018). https://doi.org/10.1016/j.fuel.2018.02.156